

**Effect of sampling time in the laboratory investigation of braided rivers**

R. Vesipa<sup>1</sup>, C. Camporeale<sup>1</sup> and L. Ridolfi<sup>1</sup>

<sup>1</sup> Department of Environment, Land and Infrastructure Engineering, Politecnico di Torino, C.so Duca degli Abruzzi 24 10129, Torino, Italy.

**Contents of this file**

- Laser triangulation of submerged targets
- Total Braiding Index and Active Braiding Index for the performed runs
- Sensitivity analysis about the precision of the bed profiling system
- Results of Runs 1 to 9
- Role of the dimensionless flow rate
- Assessment of the errors in measurements with a sampling time longer than the optimal sampling time

**Introduction**

In the Supporting Information we firstly explain the technique adopted for the laser triangulation of submerged targets.

Secondly, we report the Total Braiding Index and the Active Braiding Index of the performed runs. This information can be useful to understand the braiding intensity of the performed runs.

Thirdly, we assess the sensitivity of the results on the precision of the bed profiling system.

In the fourth place, we report the results from all the 12 performed runs. To do this, the curves showed in panels *a-d* of Figures 3-4 in the main text for run 6 are reported for all runs. Moreover, we show the same results reported in Figures 3-4 in the main text considering:

- (i) the cumulative areas  $E(t_j)$  (erosion) or  $D(t_j)$  (deposition) in place of  $R(t_j)$  (total reworking), and
- (ii) the rates  $e(t_j)$  or  $d(t_j)$  in place of  $r(t_j)$ . All the curves reported in this Supporting Information are also tabulated.

In addition, the modified versions of panels *e-f* of Figures 3-4 in the main text are shown, in which the shadings of the curve colors is given by the dimensionless flow rate,  $q$ . It should be recalled that in the main text the shadings of the curve colors is given by the dimensionless stream power,  $\omega$ .

Finally, we report a procedure that can be used to assess the errors in measurements with a sampling time longer than the optimal sampling time.

## Laser triangulation of submerged target

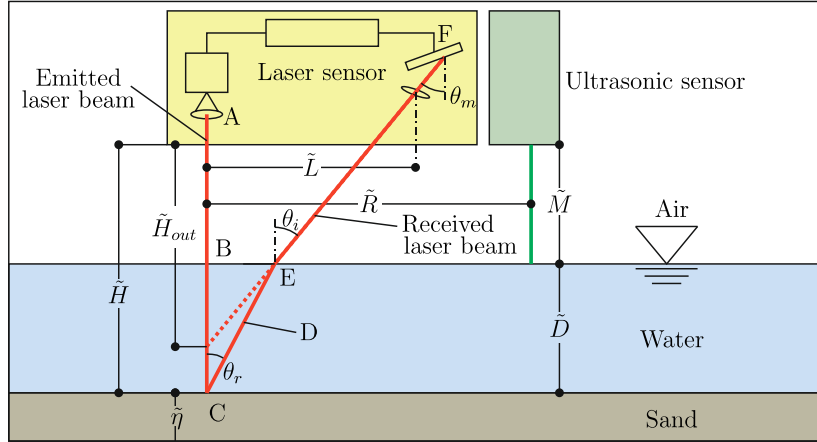


**Figure S1.** Use of a laser triangulator and an ultrasonic sensor for measuring the position of a submerged surface. It should be noted that  $\tilde{H}_{out}$  is the laser triangulator output. It is the distance between the sensor and the underwater sediment bed measured by the laser triangulator alone. It is different from the actual distance sensor- bed,  $\tilde{H}$ , because the laser beam is refracted crossing the water free surface.

Laser triangulators evaluate the distance of an object by projecting the laser beam to a target surface and by measuring the inclination of the reflected beam. They provide very precise measures when the laser beam crosses only one fluid (typically air). By contrast, they cannot be used if the target is located below the water surface.

If a triangulator is used in this context (see Figure S1), the laser beam: is emitted in air (A), crosses the water surface orthogonally (B), penetrates into water until it reaches the target (e.g., a point on a sandy bed, C), is reflected, forming an angle  $\theta_r$  with respect to the emitted beam (D), passes through the water layer with inclination  $\theta_r$ , is refracted (beam inclination increases to  $\theta_i$ ) according to Snell's law while crossing the water-air interface (E), and passes through the air layer with inclination  $\theta_i$ . Finally, it reaches the acquisition sensor (F), where  $\theta_i$  is measured. The measure from the triangulator is obtained by implementing the trigonometric relation (see Figure S1)

$$\tilde{H}_{out} = \frac{\tilde{L}}{\tan \theta_m}, \quad (1)$$

where  $\tilde{H}_{out}$  is the sensor output (the estimated sensor-surface distance),  $\theta_m$  is the inclination of the laser beam measured by the laser acquisition sensor (F), and  $\tilde{L}$  is the spacing between the laser beam emitter (A) and F.

When the laser beam targets a submerged surface, equation (1) is implemented using the post-refraction angle ( $\theta_m = \theta_i$ ) instead of the reflected angle ( $\theta_m = \theta_r$ ). Hence,  $\tilde{H}_{out}$  is underestimated (Figure S1). In order to measure submerged surfaces with triangulators, *Visconti et al.*, [2012] developed a technique aimed at correcting  $\tilde{H}_{out}$ . In particular, they demonstrated that this correction can be evaluated only if the triangulator-water surface distance ( $\tilde{M}$  in Figure 1) is measured (e.g., by an ultrasonic sensor).

In summary, the correct sensor-surface distance  $\tilde{H}$  can be obtained also for submerged surfaces, thanks to a correction of  $\tilde{H}_{out}$  based on  $\tilde{M}$ .

## Total Braiding Index and Active Braiding Index for the performed runs

The Braiding Indexes are a simple but sound metrics to characterize the braiding rivers. In particular, the Total Braiding Index (TBI) provides the number of wet channels in a cross section. On the other hand, the Active Braiding Index (ABI) provides the number of channels that transport sediments in a cross section (namely, the number of active channels) (Egozi and Ashmore, 2008).

During our experiments, we did not monitored continuously the number of active or total channels. Indeed, we made use of the well established relation between the TBI and the dimensionless flow rate,  $q$ , and between the ABI and the stream power,  $\omega$ , found by Bertoldi *et al.*, [2009].

More in detail, we performed a least-square linear-regression of the literature data relating TBI with  $q$ , and ABI with  $\omega$  (see Figures 4a and 4d in the original work of Bertoldi *et al.*, 2009). It was found that

$$TBI = 0.012 \cdot q, \quad (2)$$

$$ABI = 0.50 \cdot \omega. \quad (3)$$

Finally, we made use of (2-3) to estimate TBI and ABI from the values of  $q$  and  $\omega$  of our runs.

Figure S2 graphically shows the relations between TBI and  $q$  (panel *a*), and between ABI and  $\omega$  (panel *b*). The figure reports the original literature data by Bertoldi *et al.*, [2009] (red crosses), the least-square linear-regressions (2-3), and the indexes estimated for the runs reported in this study by equations (2-3) (blue circles). Additionally, Table S1 reports the Braiding Indexes TBI and ABI for the 12 performed runs, obtained by equations (2) and (3).

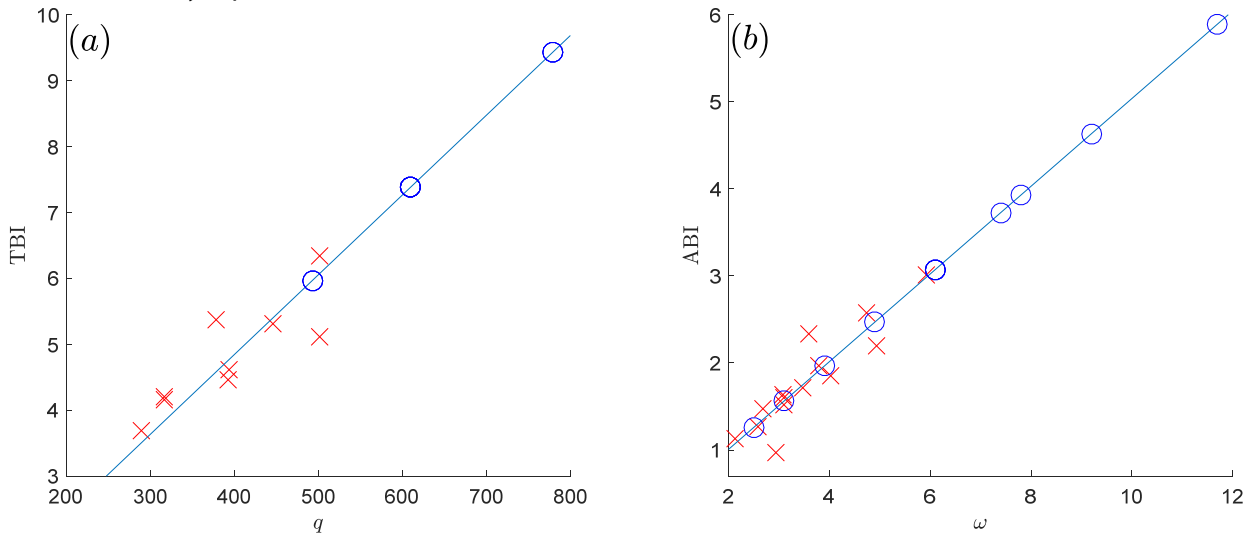


**Figure S2.** (a) Total Braiding Index as a function of the dimensionless flow rate. (b) Active Braiding Index as a function of the dimensionless stream power. The red crosses are the Indexes measured by Bertoldi *et al.*, 2009. The blue lines are the least-square linear-regressions (2-3). The blue circles are the Indexes estimated by equations (2-3) for the runs described in our study.

**Table S1.** TBI and ABI for the 12 runs reported in this study. The dimensionless flow rate,  $q$  (see equation (3d) in the main text), and the dimensionless stream power,  $\omega$  (equation (3e) in the main text) are also reported.

Run	1	2	3	4	5a	5b	5c	5d	6	7	8	9
$q$	493	610	779	493	610	610	610	610	779	493	610	779
$\omega$	2.5	3.1	3.9	4.9	6.1	6.1	6.1	6.1	7.8	7.4	9.2	11.7
TBI	6.0	7.4	9.4	6.0	7.4	7.4	7.4	7.4	9.4	6.0	7.4	9.4
ABI	1.3	1.6	2.0	2.5	3.1	3.1	3.1	3.1	3.9	3.7	4.6	5.9

### Sensitivity analysis about the precision of the bed profiling system

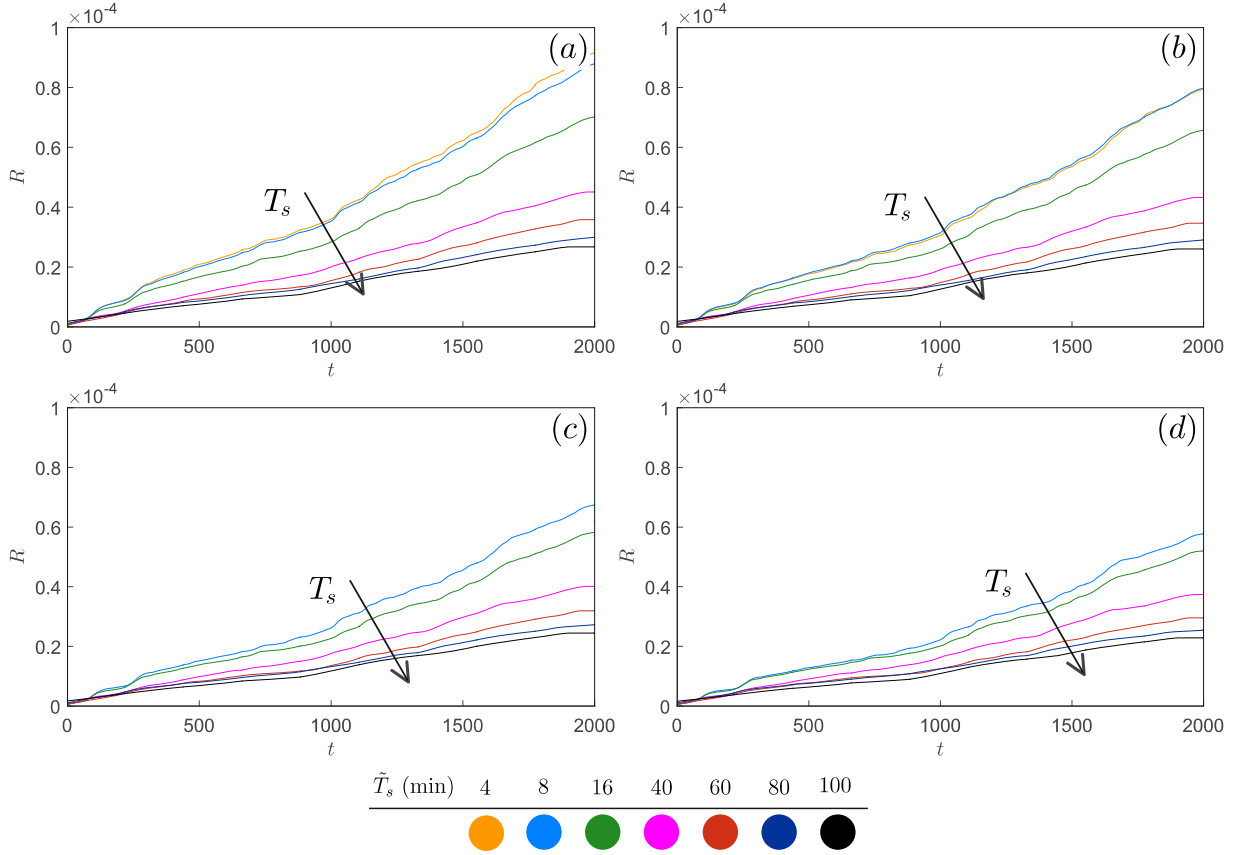


**Figure S3.** Total reworked area,  $R(t_j)$  evaluated with different precisions of the bed profiling system,  $\tilde{\delta}$ . (a)  $\tilde{\delta} = 0.5 \text{ mm} = \tilde{d}_{50}$ . (b)  $\tilde{\delta} = 1.0 \text{ mm} = 2\tilde{d}_{50}$ . (c)  $\tilde{\delta} = 1.5 \text{ mm} = 3\tilde{d}_{50}$ . (d)  $\tilde{\delta} = 2.0 \text{ mm} = 4\tilde{d}_{50}$ . Data are from Run 6.

Figure S3 shows four versions of the Figure 3a reported in the main manuscript. In particular, the figures refer to the cumulated reworked area,  $R(t_j)$ , evaluated as a function of the survey frequency  $T_s$  (different colors, see equation 6a in the main manuscript for the definition) and for different precisions of the bed profiling system,  $\tilde{\delta}$  (different panels). See Section 3.1 of the main manuscript for the definition of  $\tilde{\delta}$ .

Two key behaviors stand out. First, for high values of  $T_s$  ( $T_s \geq 40$  min, magenta line) a reduction of the precision of the bed profiling system does not impact the curves  $R(t_j)$ . Second, for low values of  $T_s$  ( $T_s < 40$  min) a reduction of the precision of the bed profiling system impacts to a great extent the curves  $R(t_j)$ . In particular, a strong reduction of the reworked volume is observed when instrument precision is reduced. For instance, the reworked volume evaluated for  $T_s = 4$  min reduces from  $9 \cdot 10^{-5}$  (panel a) to  $6 \cdot 10^{-5}$  if  $\tilde{\delta}$  is increased from 0.5 to 2.0 mm (panel S3b).

This behavior clearly shows that the survey precision is a crucial parameter in the measurement procedure. In fact, if the measurement system cannot detect changes below a certain resolution, more frequent surveys deliver no new information. Hence, surveys with high frequency require the measurement of bed elevation alterations with high precision. However, bed elevation alterations are

strongly influenced by the sediment bed roughness. A sediment bed made up of grains with mean diameter  $\tilde{d}_{50}$  exhibits elevation alterations of the orders of  $\tilde{d}_{50}$  or multiples. In fact the bed elevation alterations occur because one (ore more) grain is added ( $\Delta\tilde{\eta} = +\tilde{d}_{50}$ ) in – or is removed ( $\Delta\tilde{\eta} = -\tilde{d}_{50}$ ) from – a given plot. It follows that precisions much larger than the mean sediment grain diameter (i.e.,  $\tilde{\delta} \ll \tilde{d}_{50}$ ) does not add new information about the bed morphological evolution, as the morphological evolution takes place through alterations of the order of  $\tilde{d}_{50}$ .

Run 1

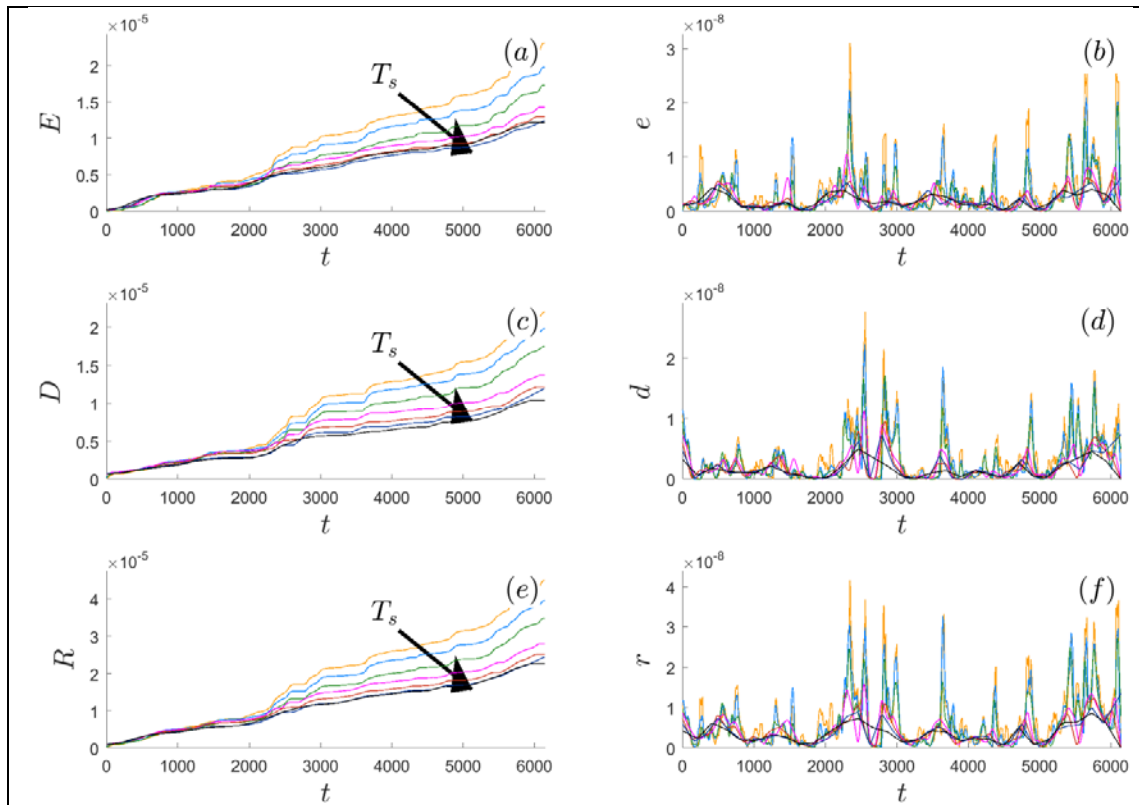


**Figure S4.** (a,b) Cumulative eroded area,  $E(t_j)$ , and eroding rate,  $e(t_j)$ . (c,d) Cumulative deposited area,  $D(t_j)$ , and depositing rate,  $d(t_j)$ . (e,f) Cumulative reworked area,  $R(t_j)$ , and reworking rate,  $r(t_j)$ . Colors refers to  $\tilde{T}_s$ : orange 4 min, light blue 8 min, green 16 min, magenta 40 min, red 60 min, blue 80 min, black 100 min. Data are from run 1.

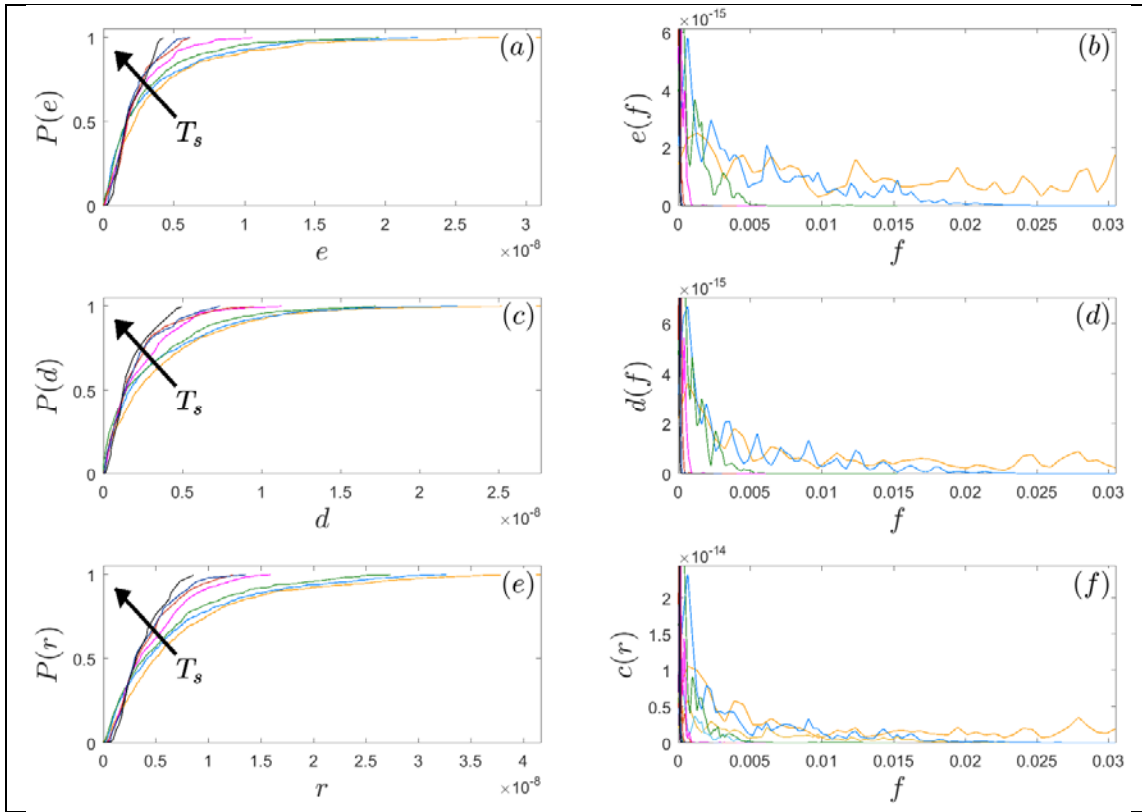


**Figure S5.** (a,b) CDF and spectrum of  $e(t_j)$ . (c,d) CDF and spectrum of  $d(t_j)$ . (e,f) CDF and spectrum of  $r(t_j)$ . Colors refers to  $\tilde{T}_s$ : orange 4 min, light blue 8 min, green 16 min, magenta 40 min, red 60 min, blue 80 min, black 100 min. Data are from run 1.

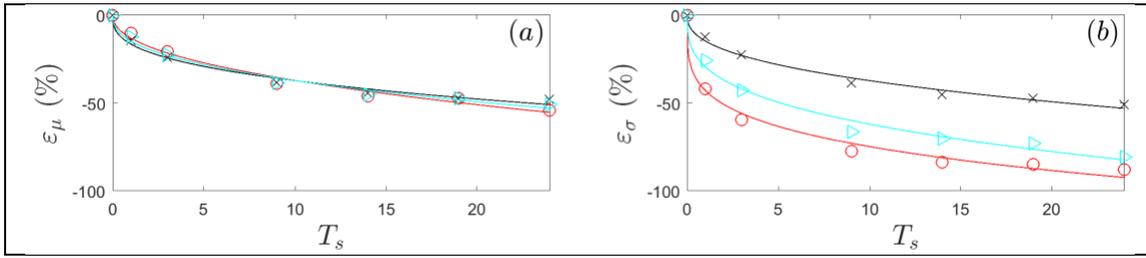


**Figure S6.** The  $T_s$ -dependent errors  $\varepsilon_\mu$  (a) and  $\varepsilon_\sigma$  (b). The black lines and crosses refers to the erosion rate, the red lines and circles refer to the deposition rate, and the blue lines and triangles refer to the total reworking rate. Data are from run 1.

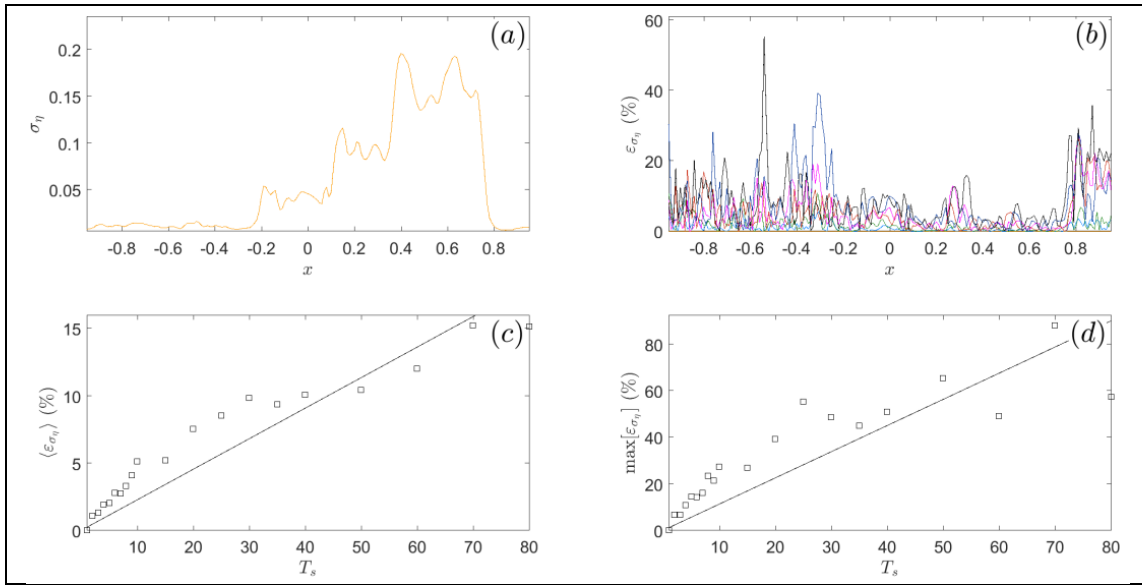


**Figure S7.** (a)  $\sigma_\eta(x, T_s)$  for  $T_s = T_{s,\min} = 1$ . (b)  $\varepsilon_{\sigma_\eta}(x)$ . Colors refers to  $\tilde{T}_s$ : orange 4 min, light blue 8 min, green 16 min, magenta 40 min, red 60 min, blue 80 min, black 100 min. (c,d)  $\langle \varepsilon_{\sigma_\eta} \rangle$  and  $\max[\varepsilon_{\sigma_\eta}(x)]$  as a function of  $T_s$ . The straight lines qualitatively show the trend errors, and were obtained by a least square interpolation of the data. Data are from run 1.

Run 2

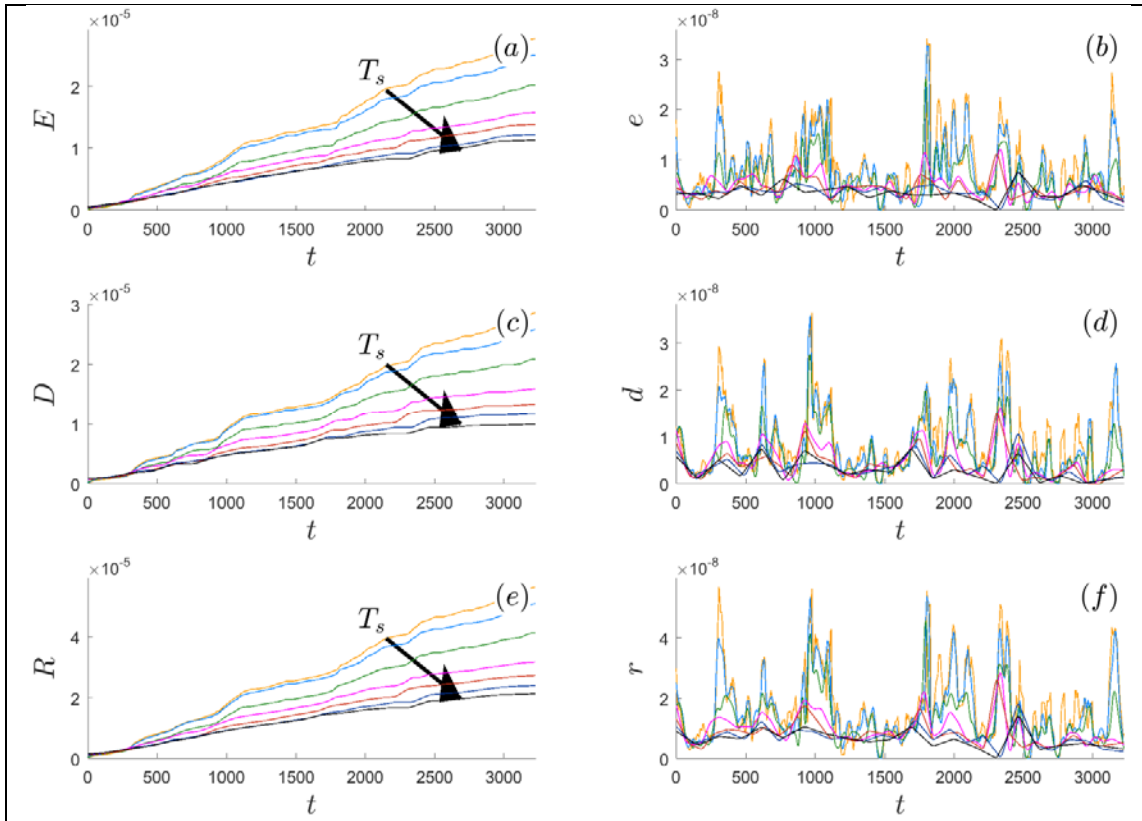


Figure S8. Data are from run 2. See Figure S2 for explanation.

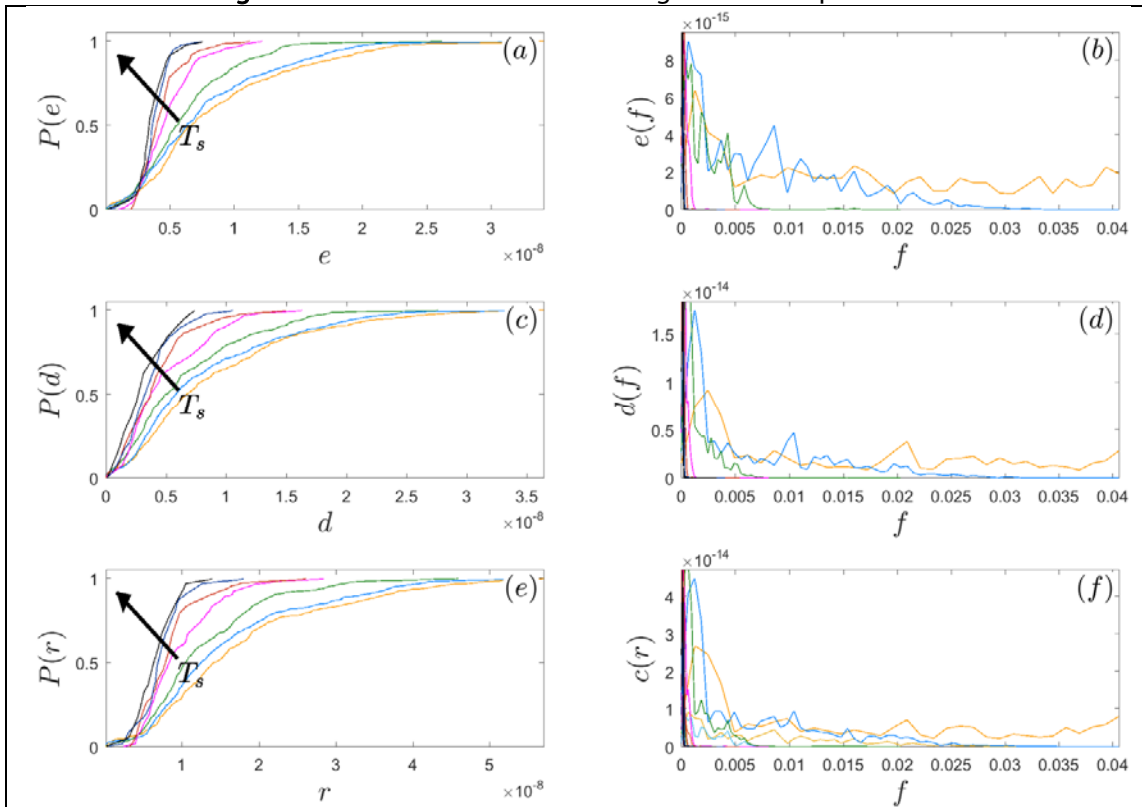
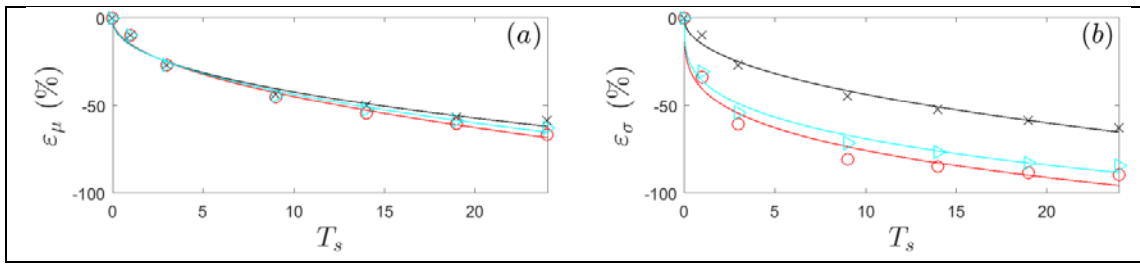
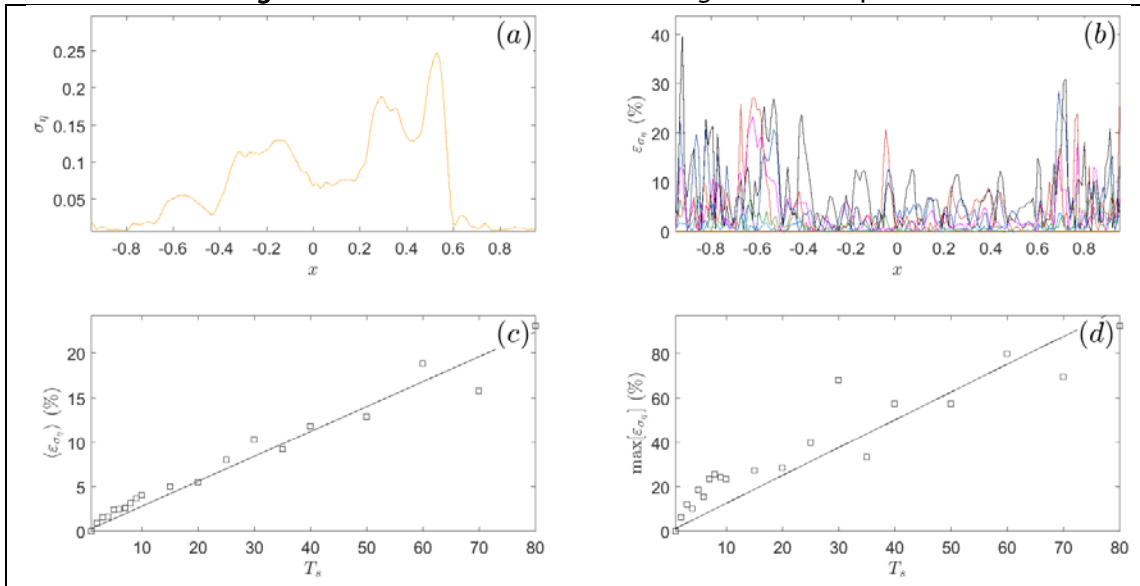


Figure S9. Data are from run 2. See Figure S3 for explanation.



**Figure S10 .** Data are from run 2. See Figure S4 for explanation.



**Figure S11.** Data are from run 2. See Figure S5 for explanation.

Run 3

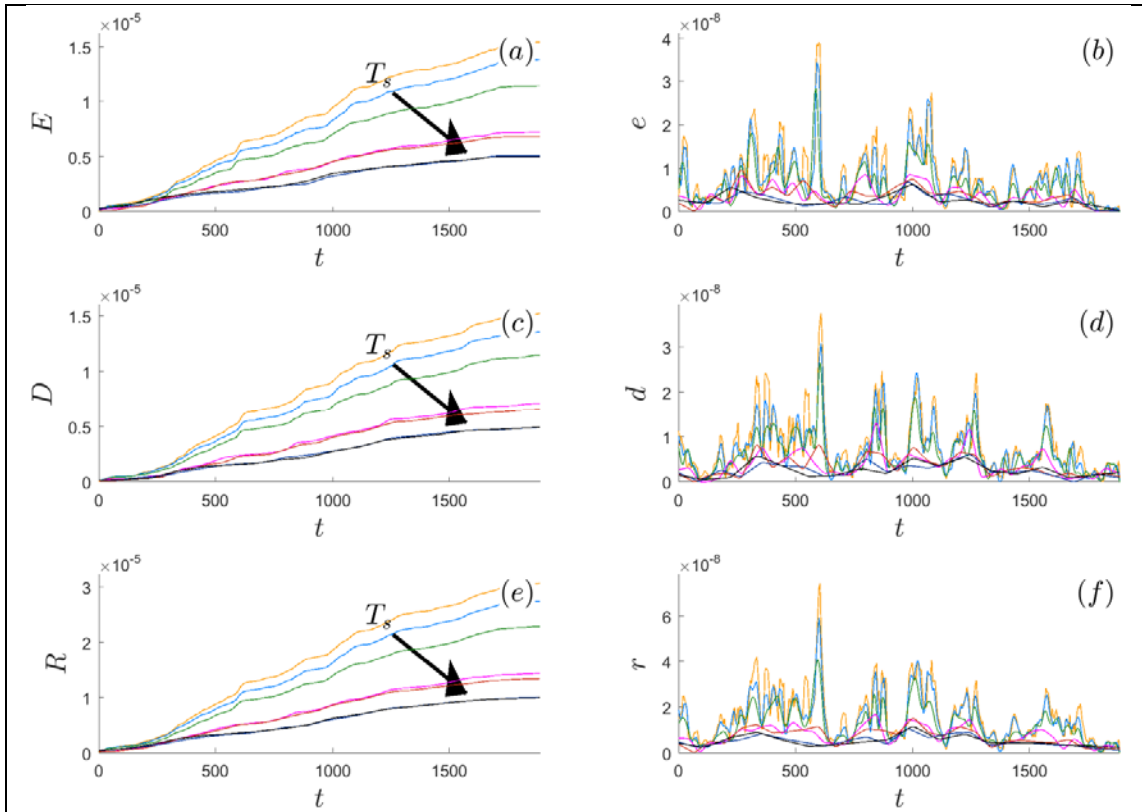


Figure S12 . Data are from run 3. See Figure S2 for explanation.

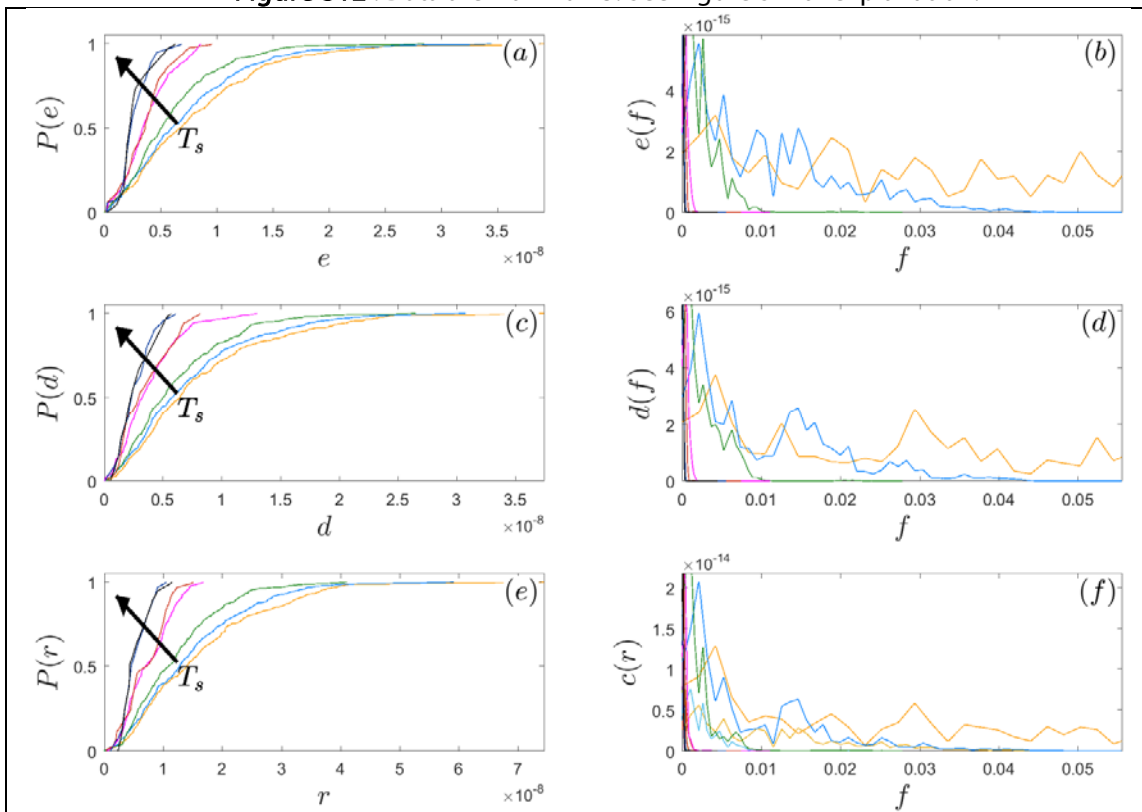


Figure S13 . Data are from run 3. See Figure S3 for explanation.

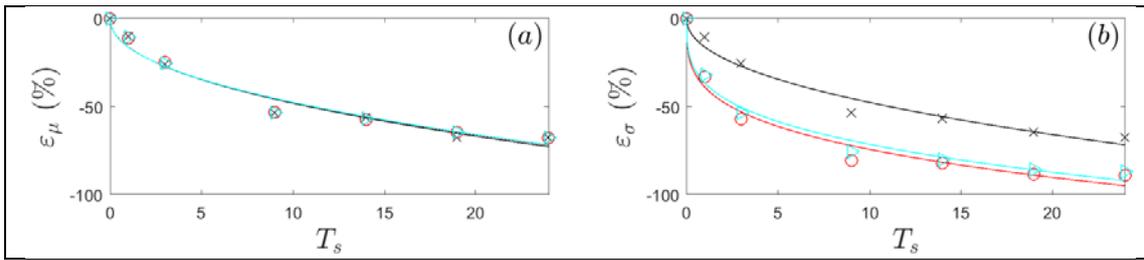


Figure S14 . Data are from run 3. See Figure S4 for explanation.

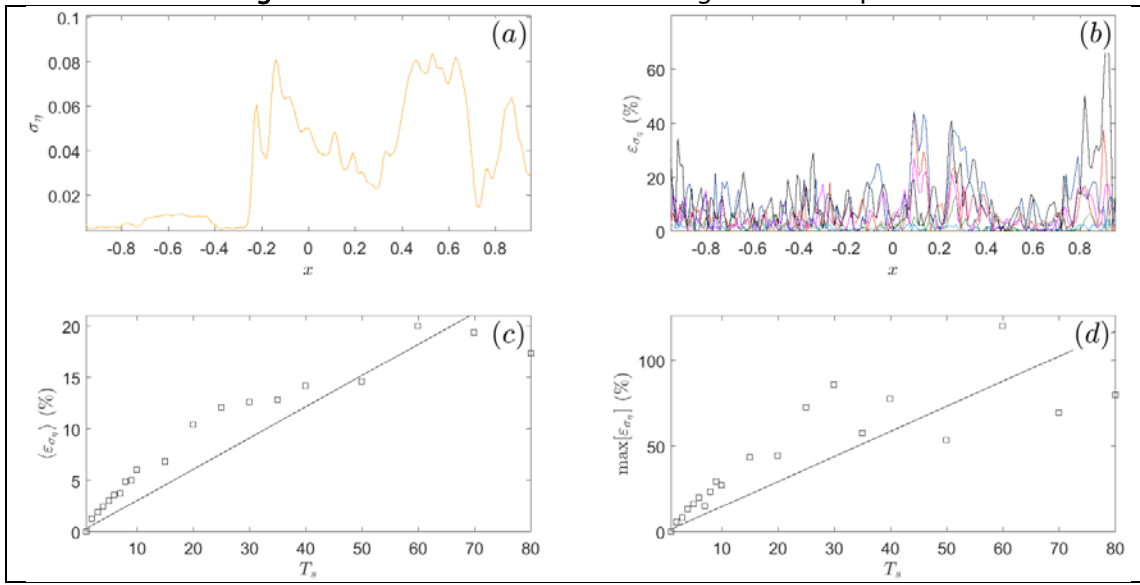


Figure S15 . Data are from run 3. See Figure S5 for explanation.

Run 4

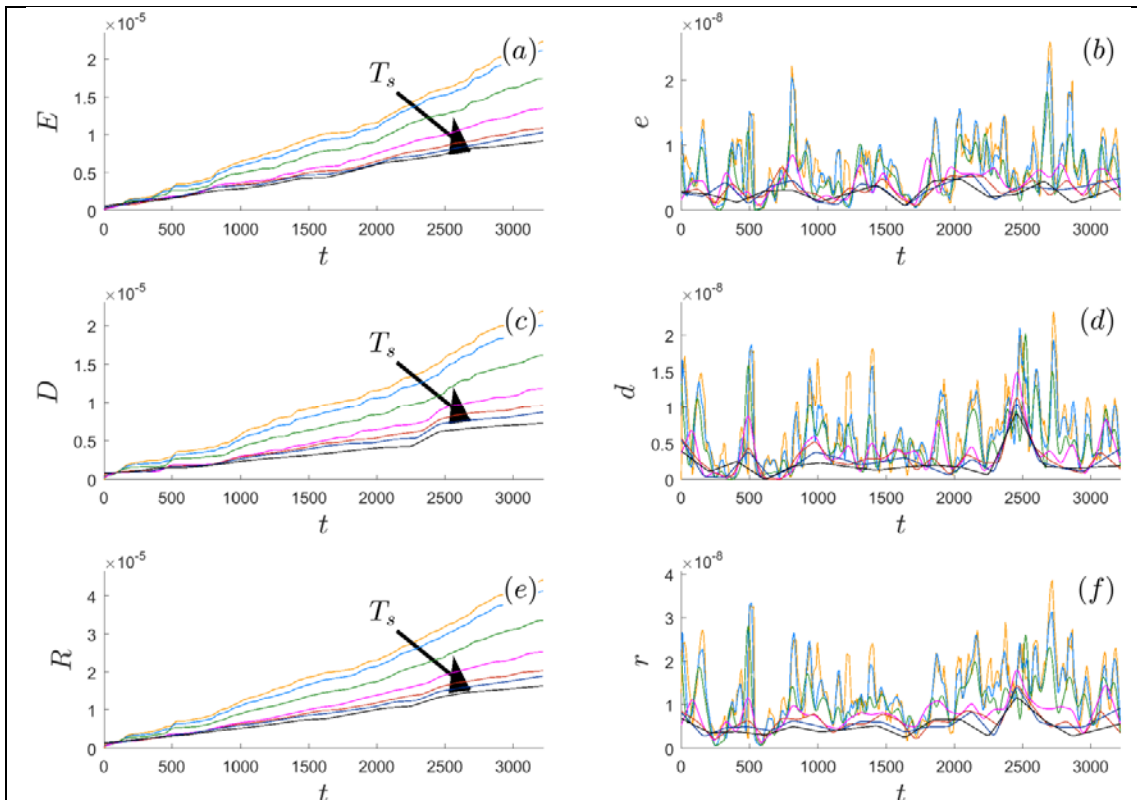


Figure S16 . Data are from run 4. See Figure S2 for explanation.

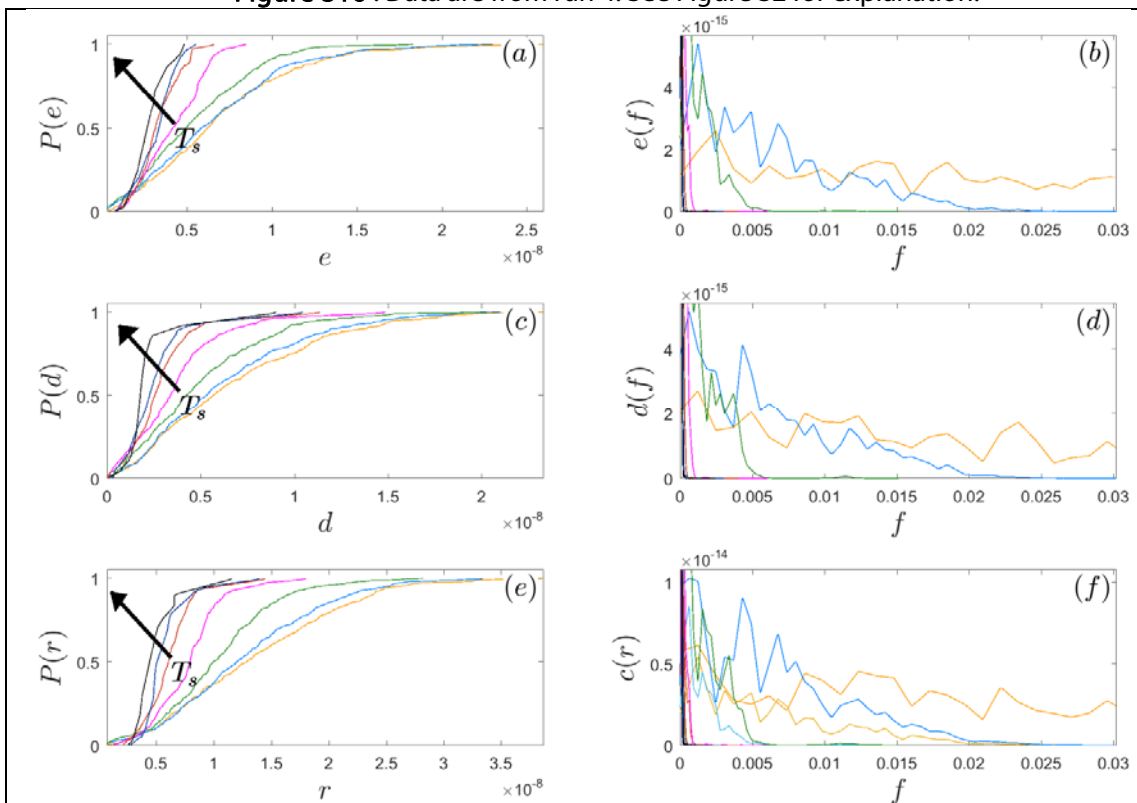


Figure S17 . Data are from run 4. See Figure S3 for explanation.

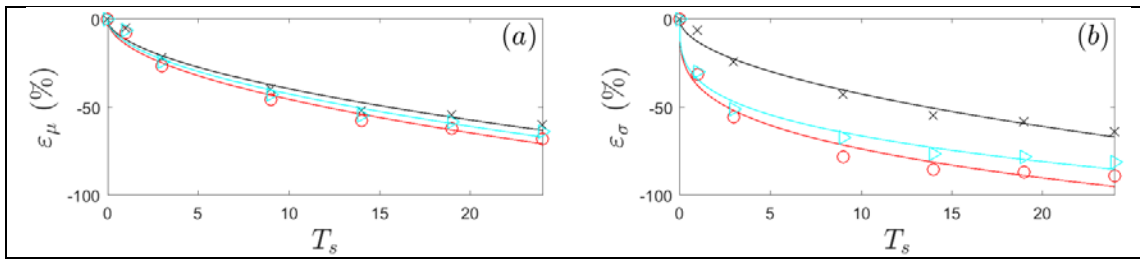


Figure S18 . Data are from run 4. See Figure S4 for explanation.

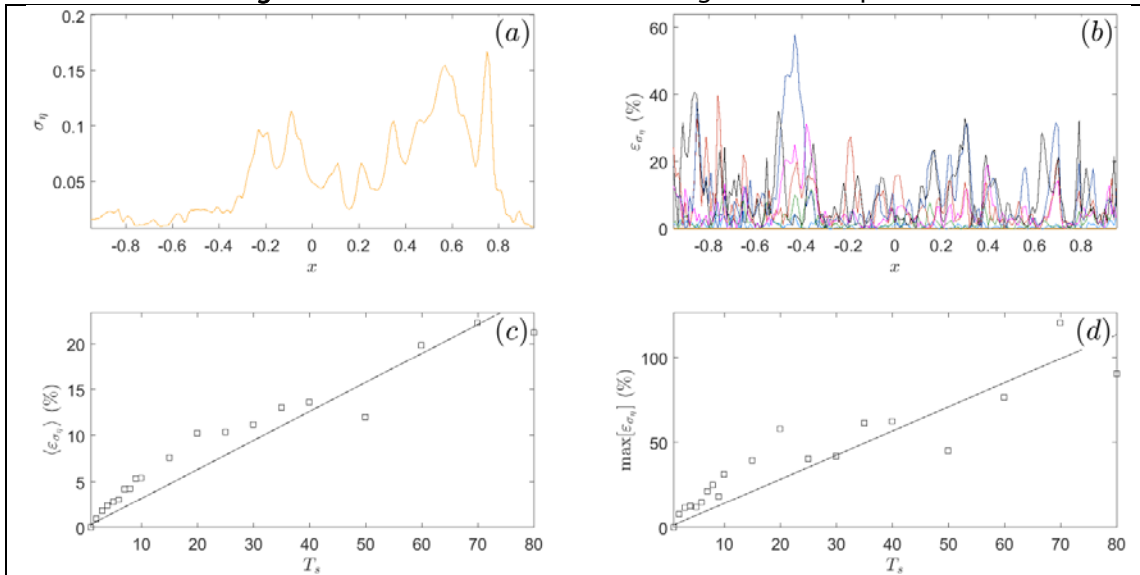


Figure S19 . Data are from run 4. See Figure S5 for explanation.

Run 5a

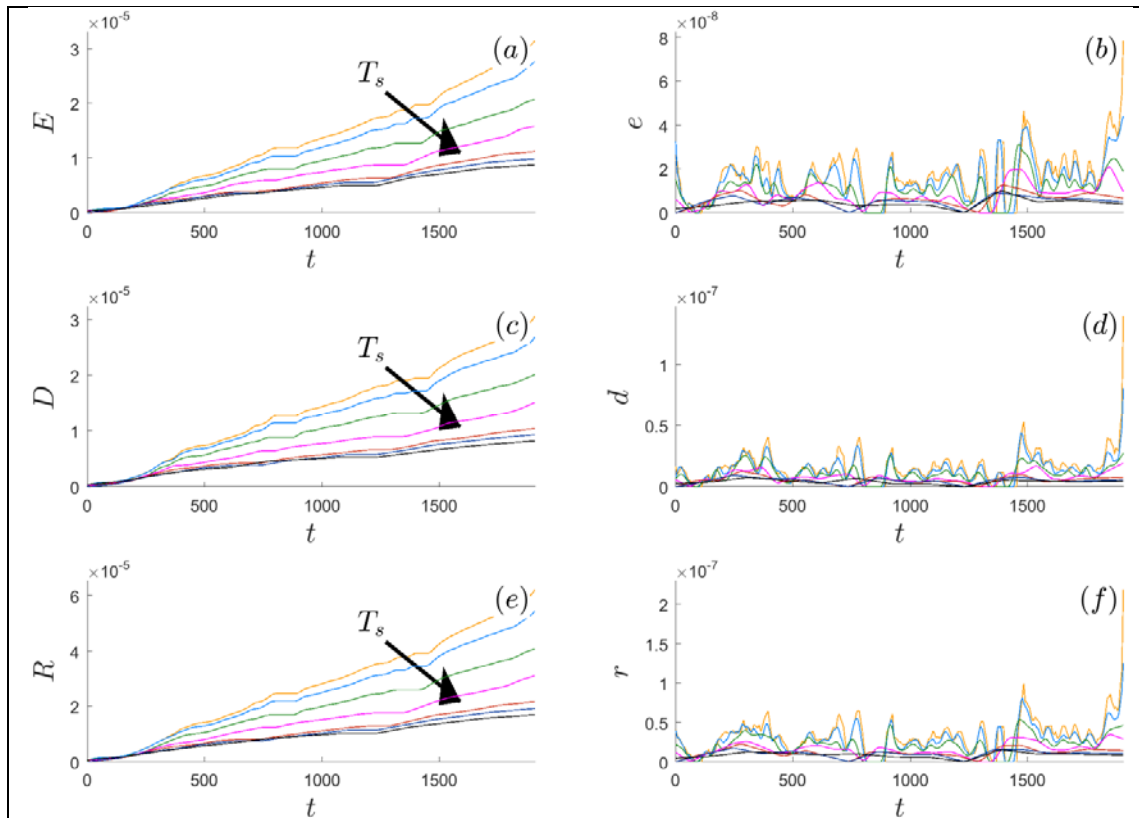


Figure S20 . Data are from run 5a. See Figure S2 for explanation.

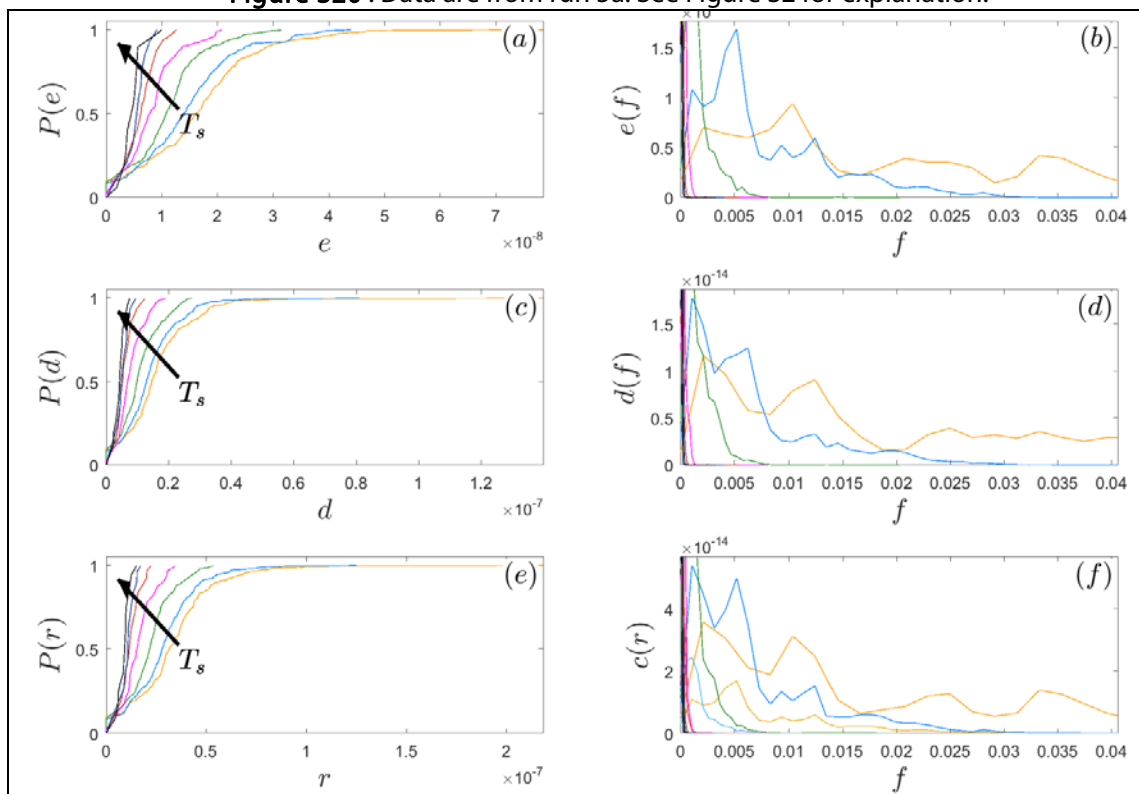


Figure S21 . Data are from run 5a. See Figure S3 for explanation.

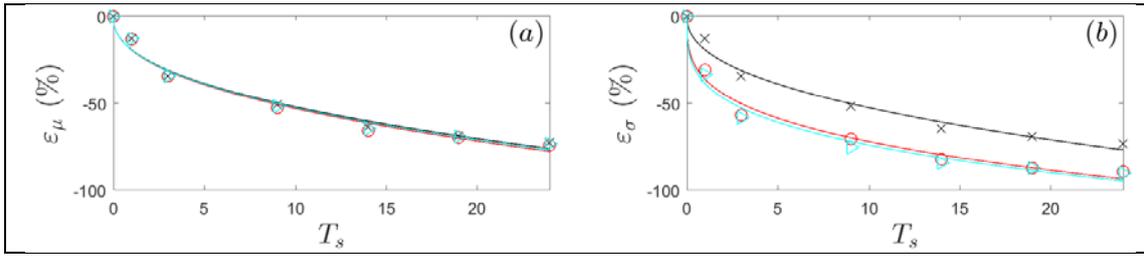


Figure S22 . Data are from run 5a. See Figure S4 for explanation.

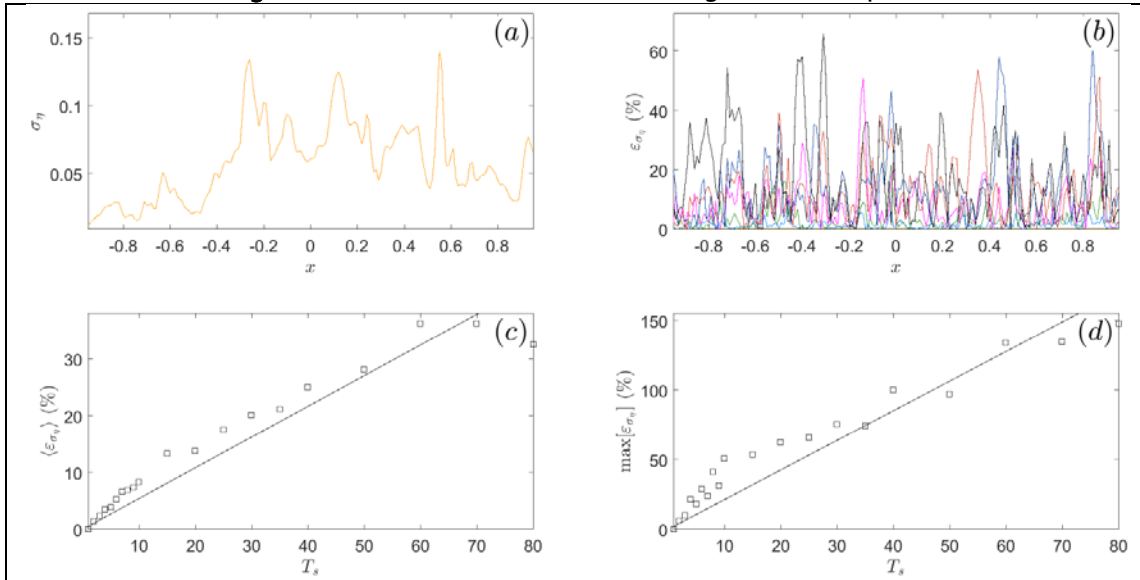


Figure S23 . Data are from run 5a. See Figure S5 for explanation.

Run 5b

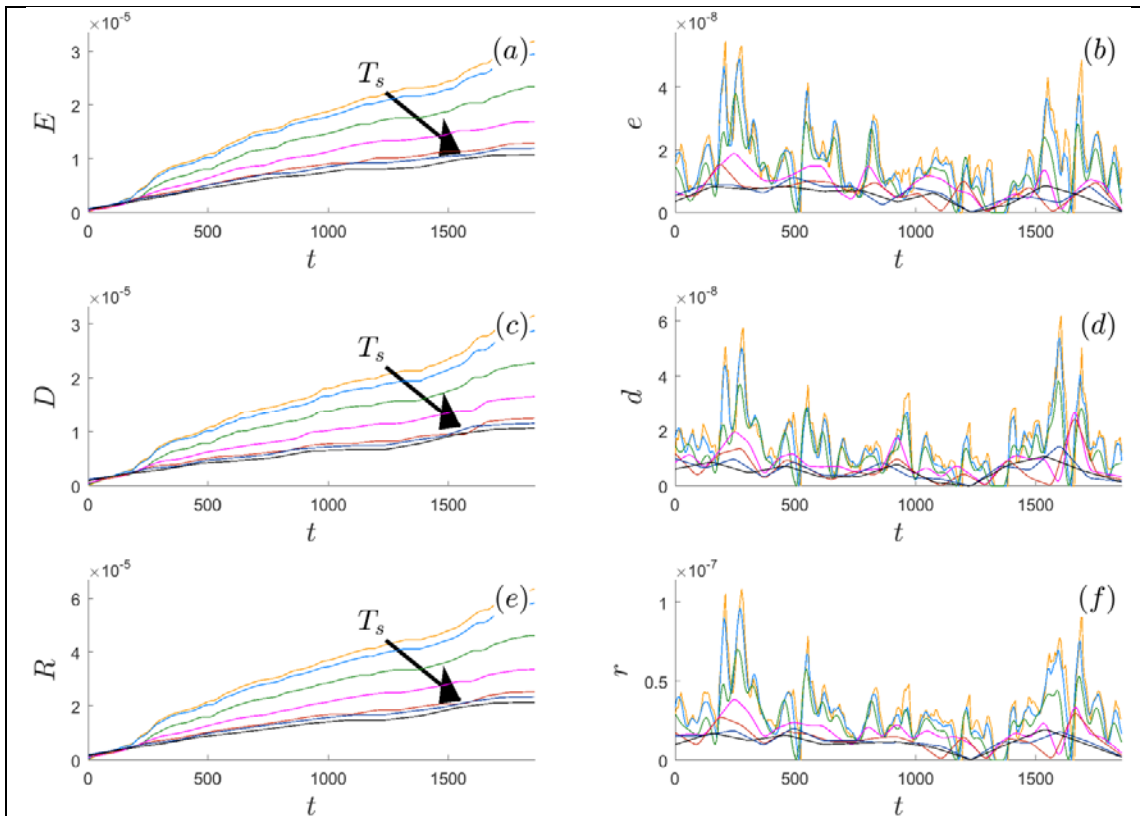


Figure S24 . Data are from run 5b. See Figure S2 for explanation.

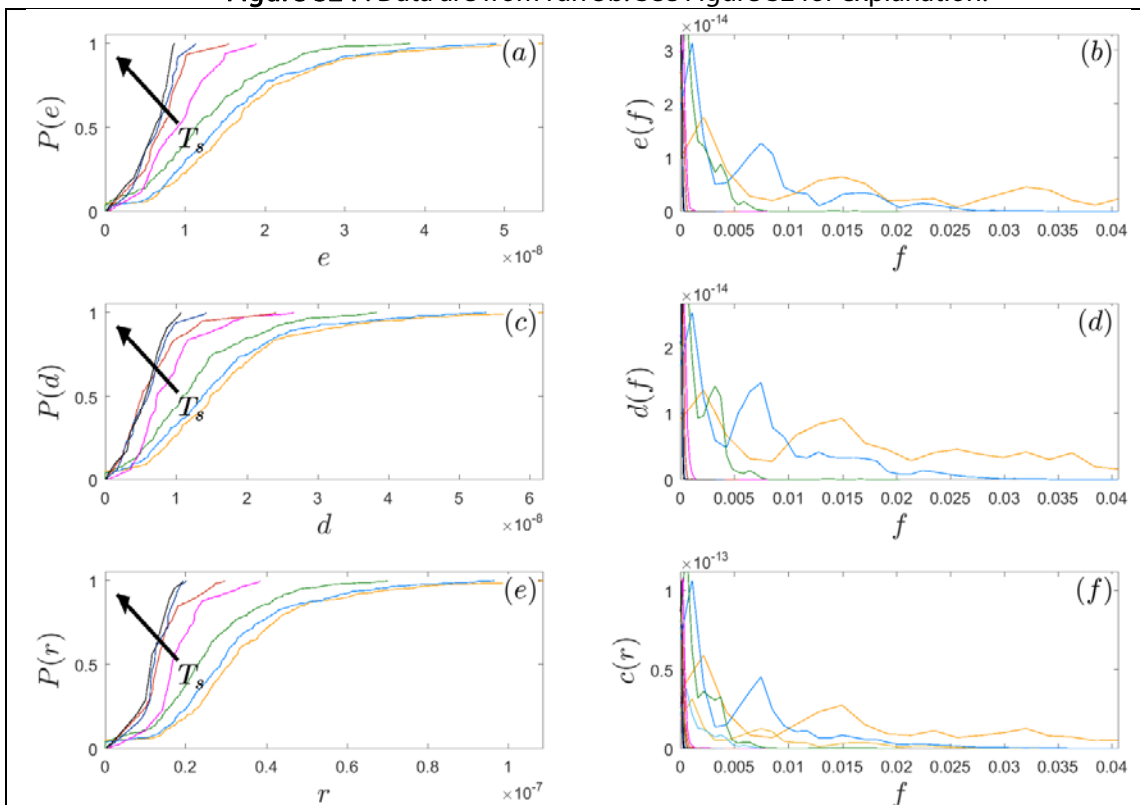


Figure S25 . Data are from run 5b. See Figure S3 for explanation.

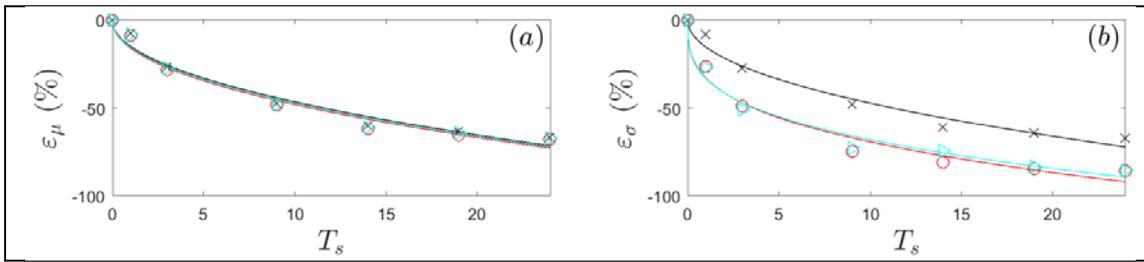


Figure S26 . Data are from run 5b. See Figure S4 for explanation.

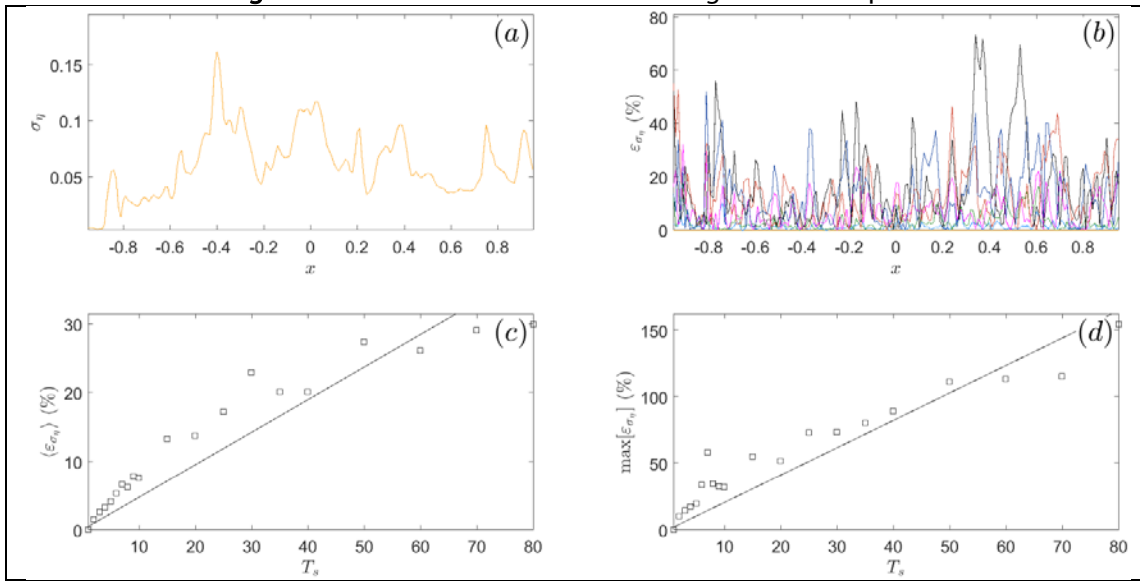


Figure S27 . Data are from run 5b. See Figure S5 for explanation.

Run 5c

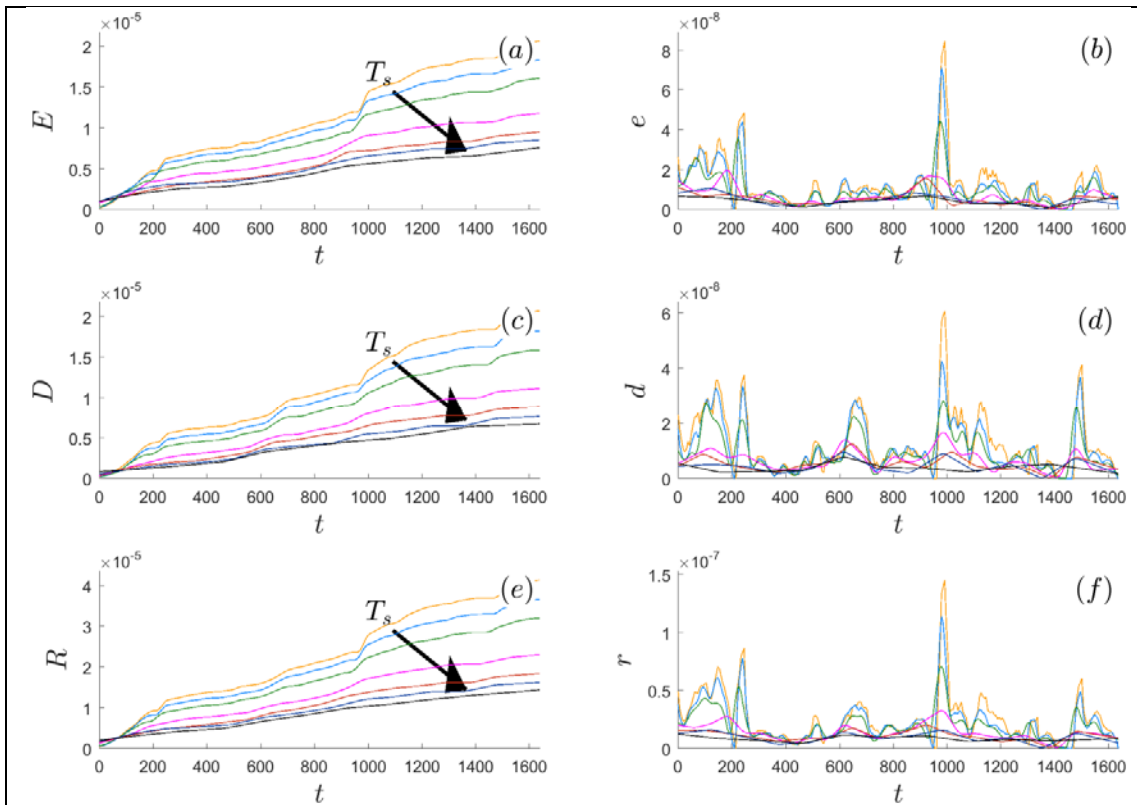


Figure S28 . Data are from run 5c. See Figure S2 for explanation.

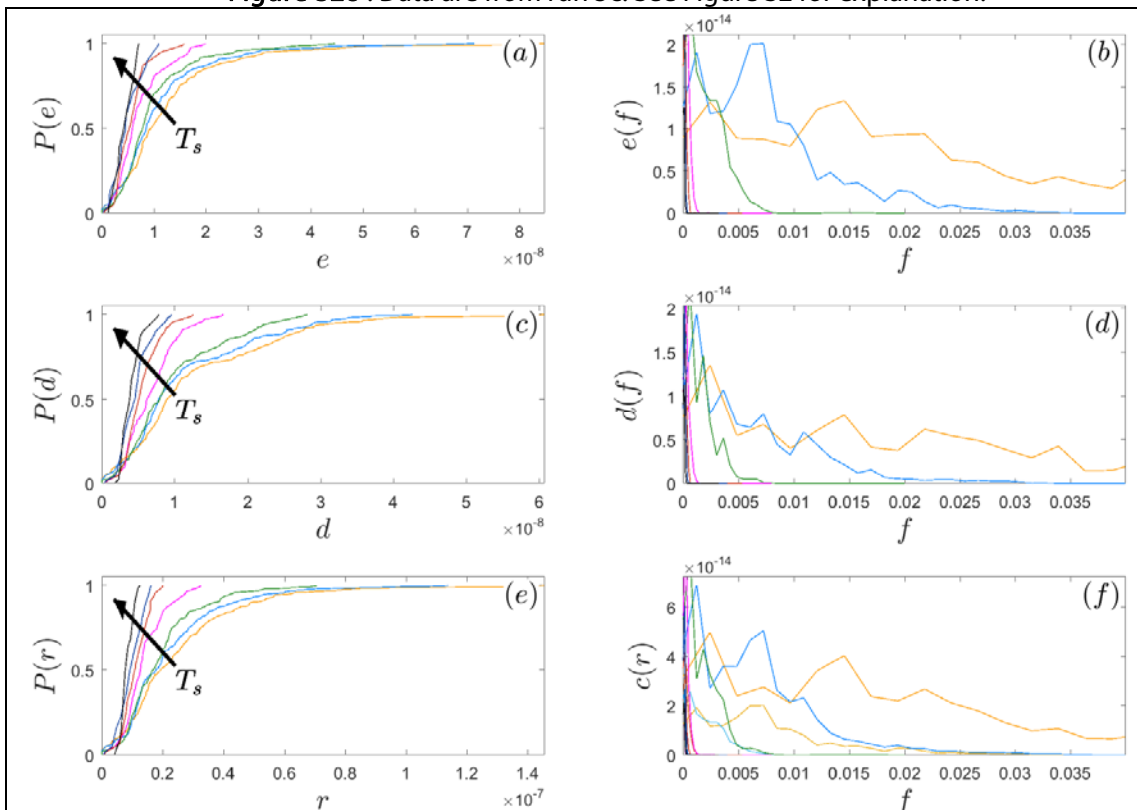


Figure S29. Data are from run 5c. See Figure S3 for explanation.

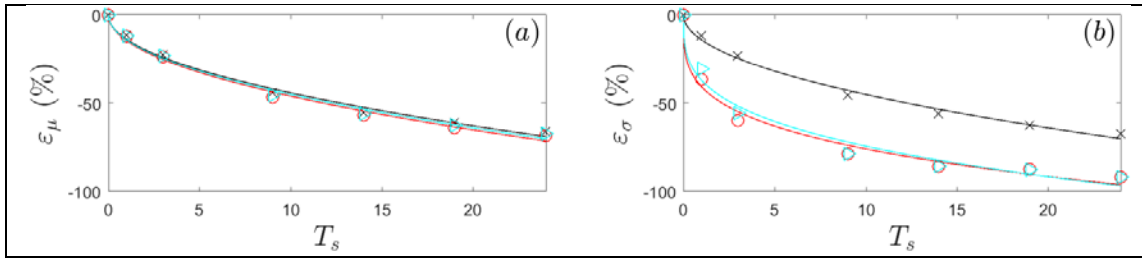


Figure S30 . Data are from run 5c. See Figure S4 for explanation.

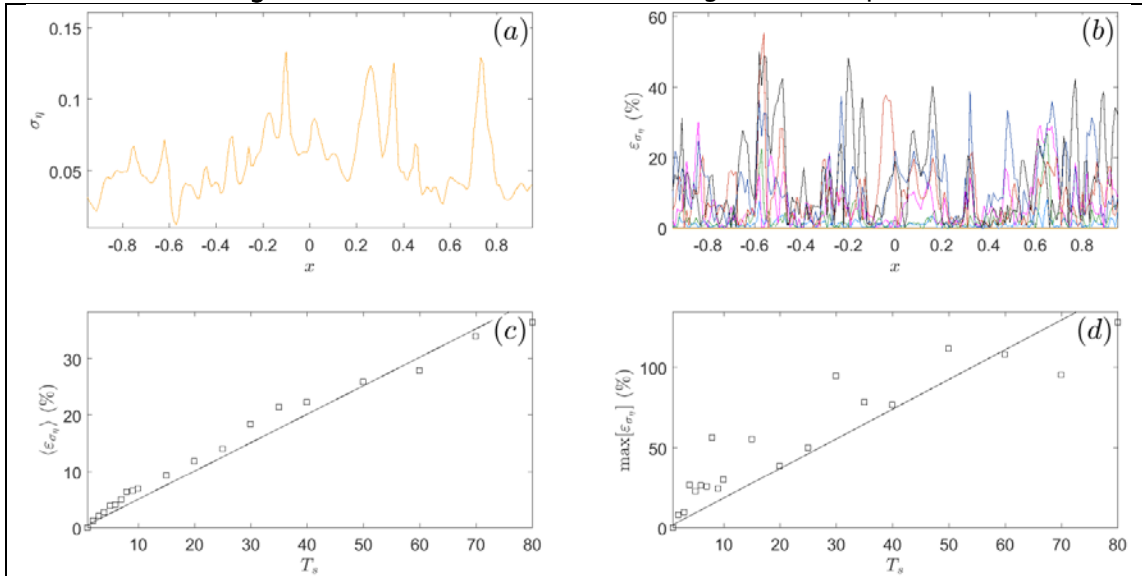


Figure S31 . Data are from run 5c. See Figure S5 for explanation.

Run 5d

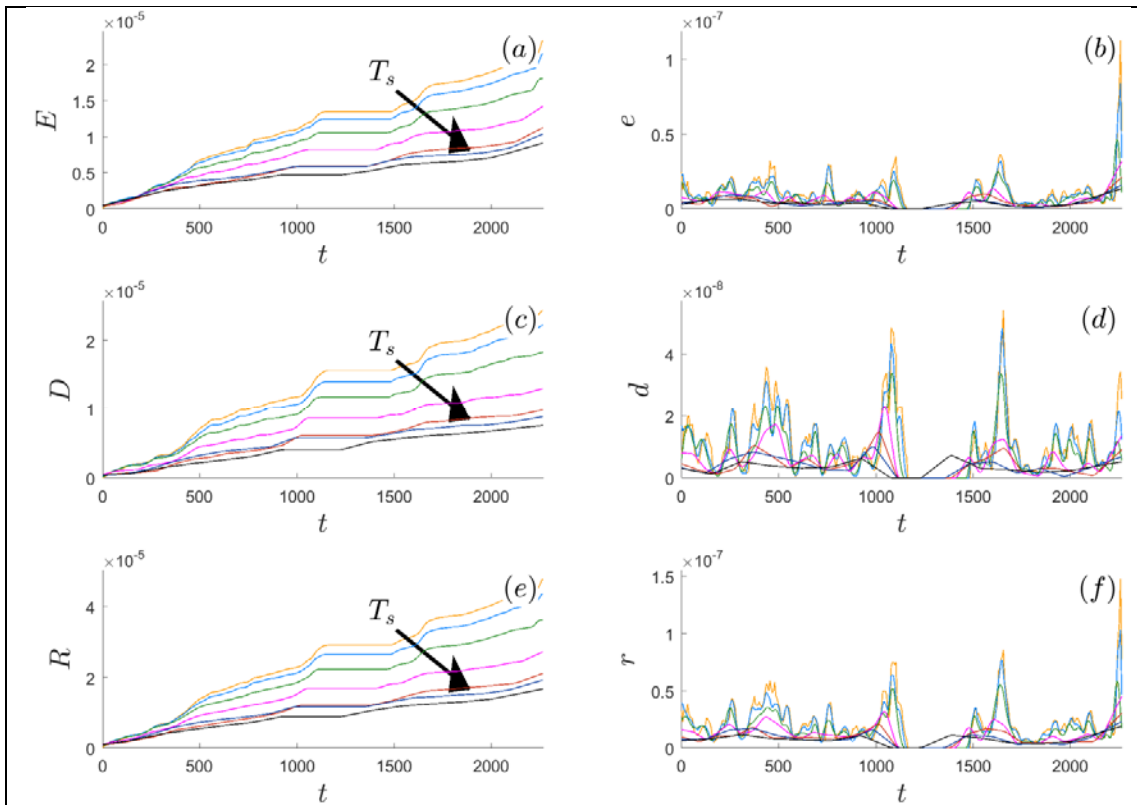


Figure S32 . Data are from run 5d. See Figure S2 for explanation.

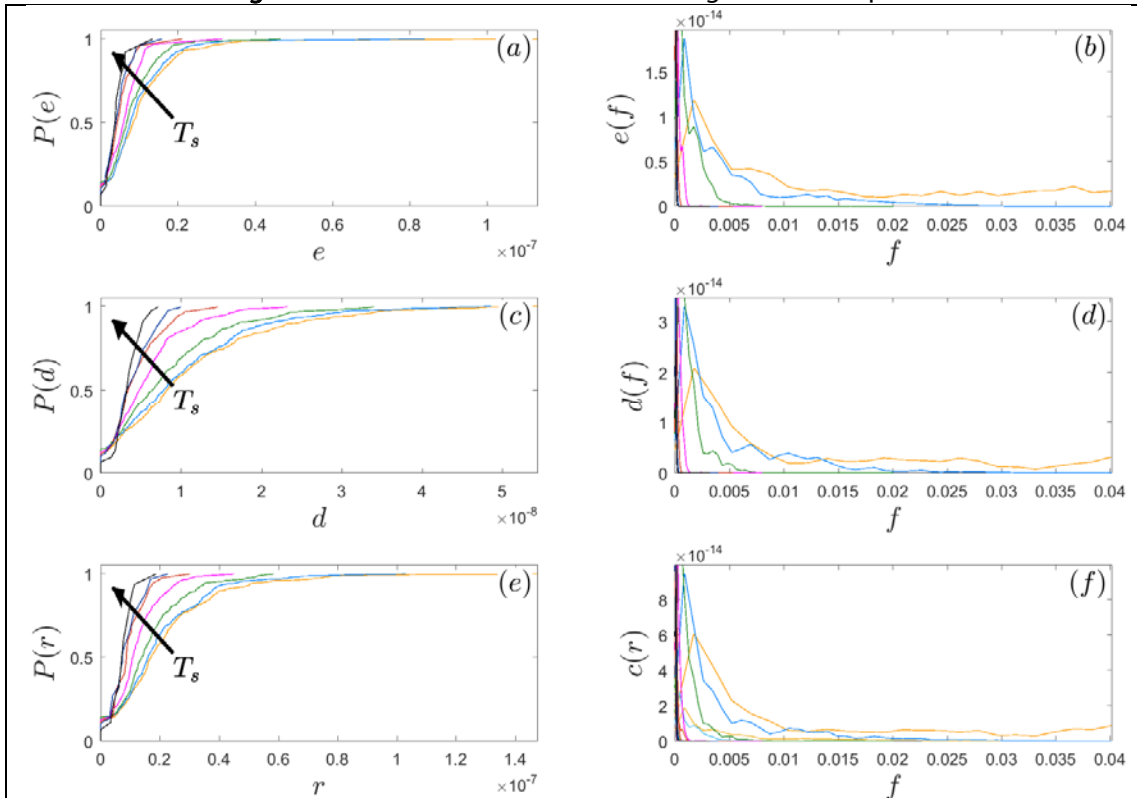


Figure S33 . Data are from run 5d. See Figure S3 for explanation.

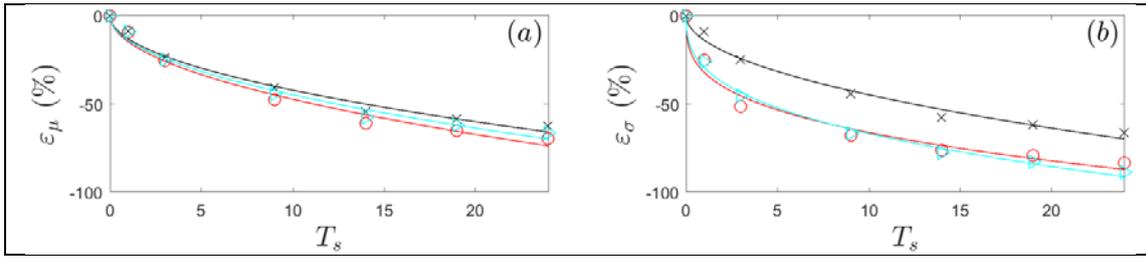


Figure S34 . Data are from run 5d. See Figure S4 for explanation.

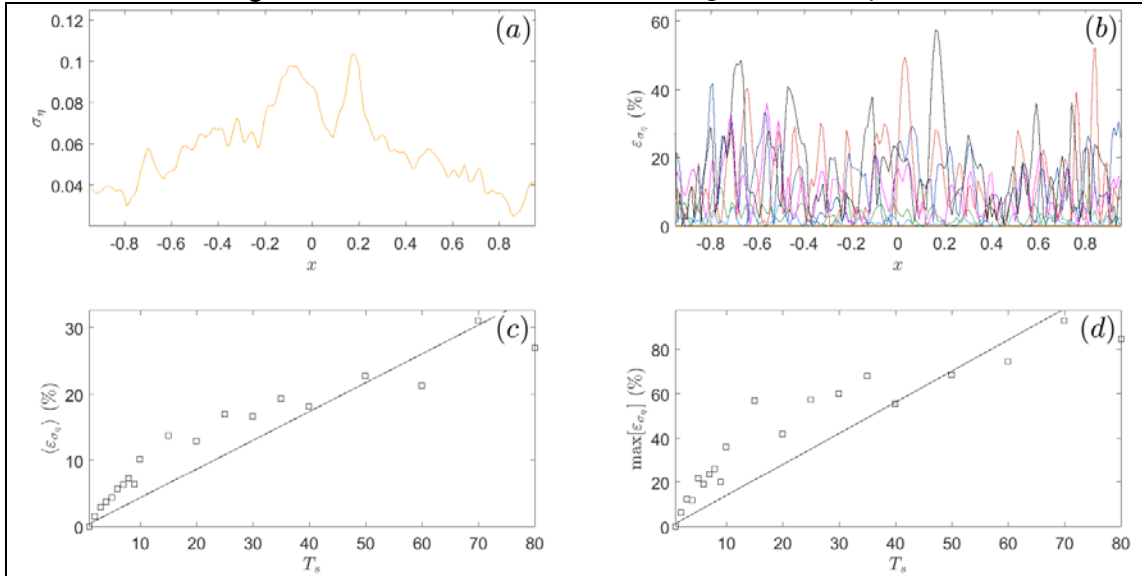


Figure S35 . Data are from run 5d. See Figure S5 for explanation.

Run 6

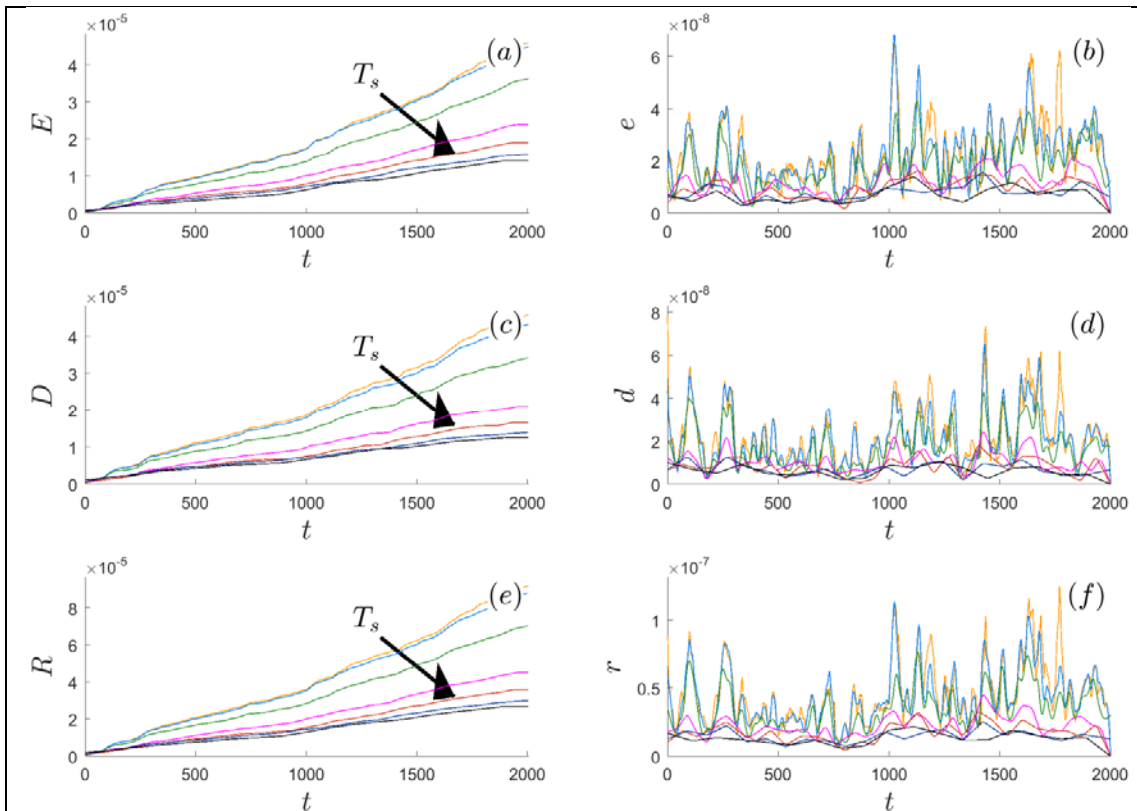


Figure S36 . Data are from run 6. See Figure S2 for explanation.

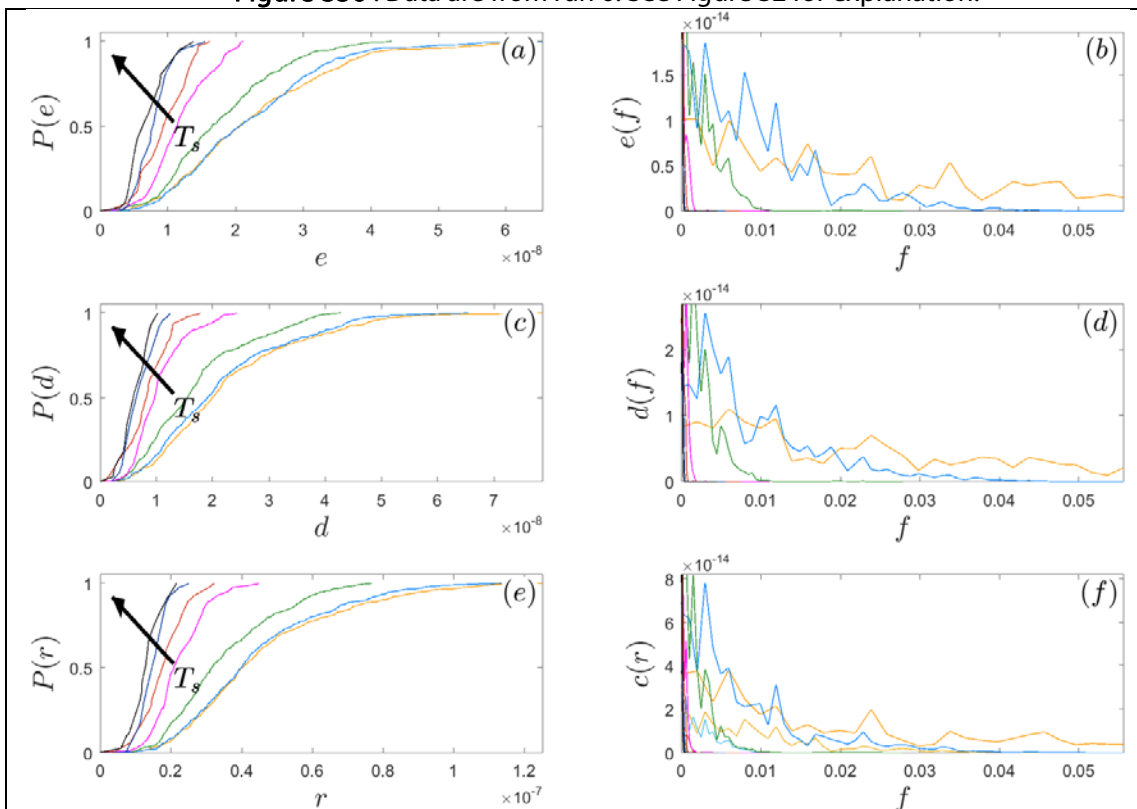


Figure S37 . Data are from run 6. See Figure S3 for explanation.

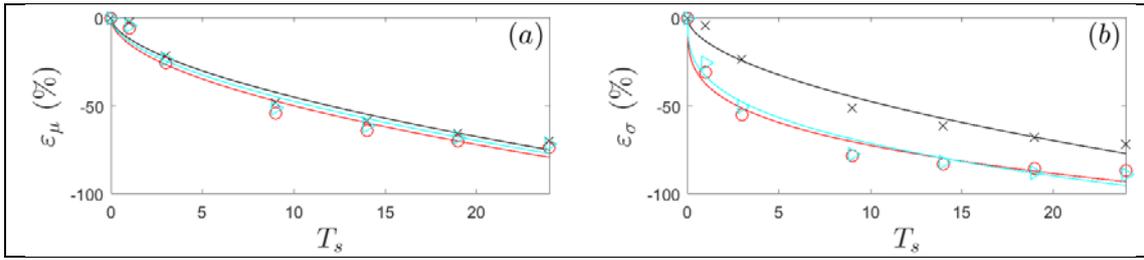


Figure S38 . Data are from run 6. See Figure S4 for explanation.

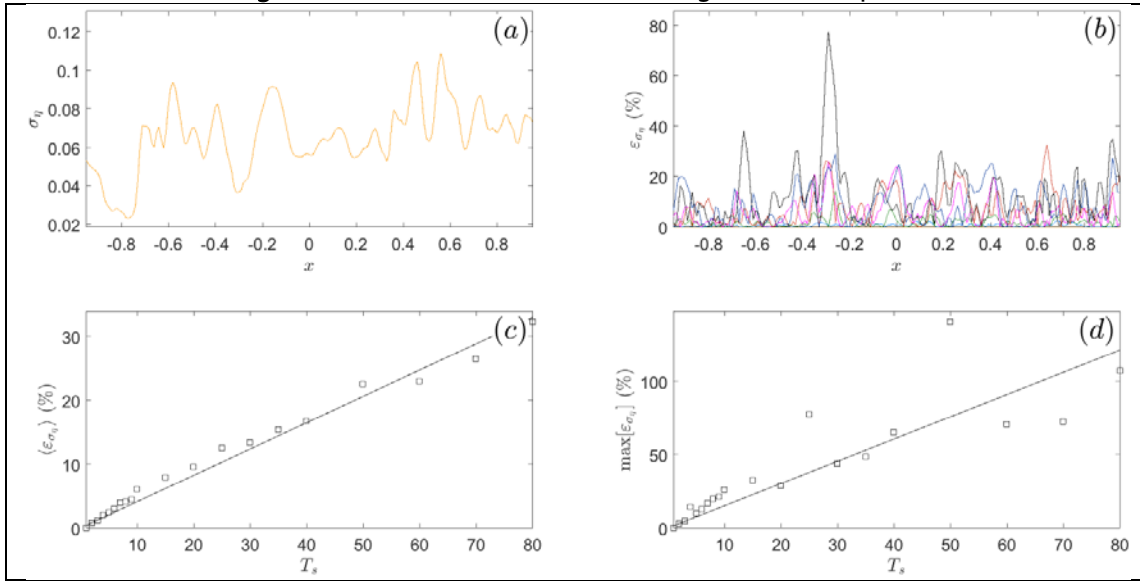


Figure S39. Data are from run 6. See Figure S5 for explanation.

Run 7

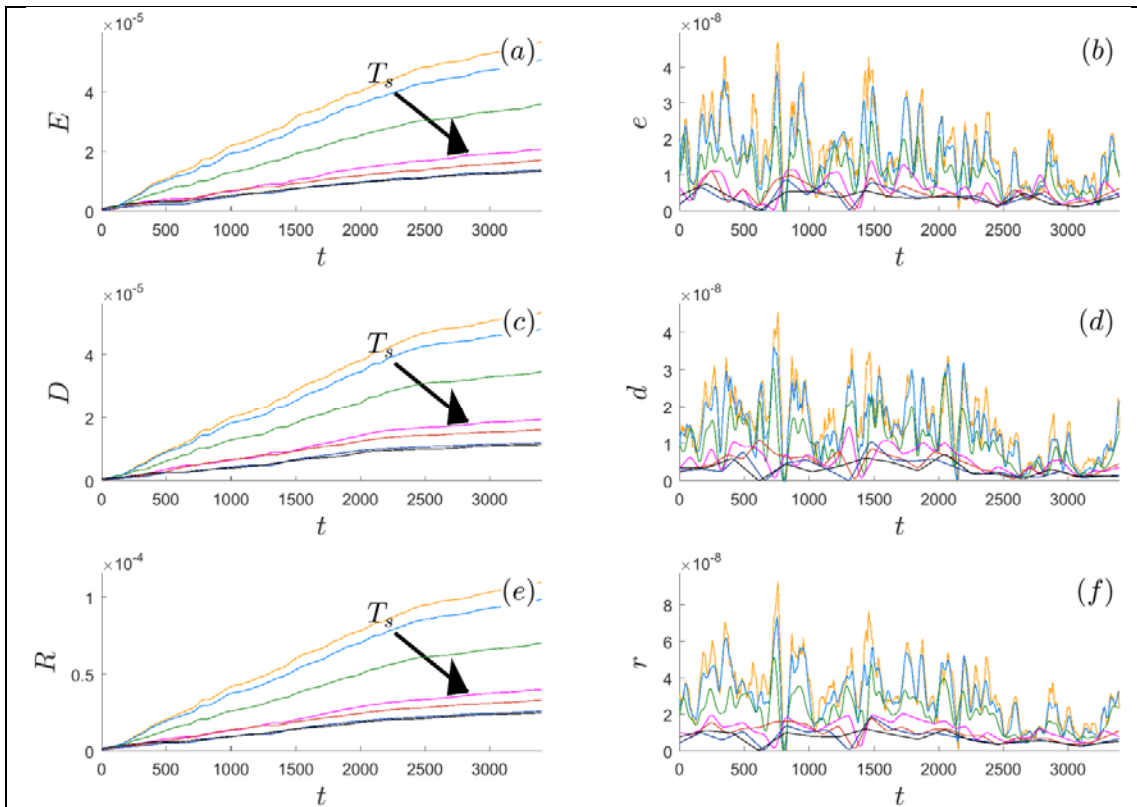


Figure S40 . Data are from run 7. See Figure S2 for explanation.

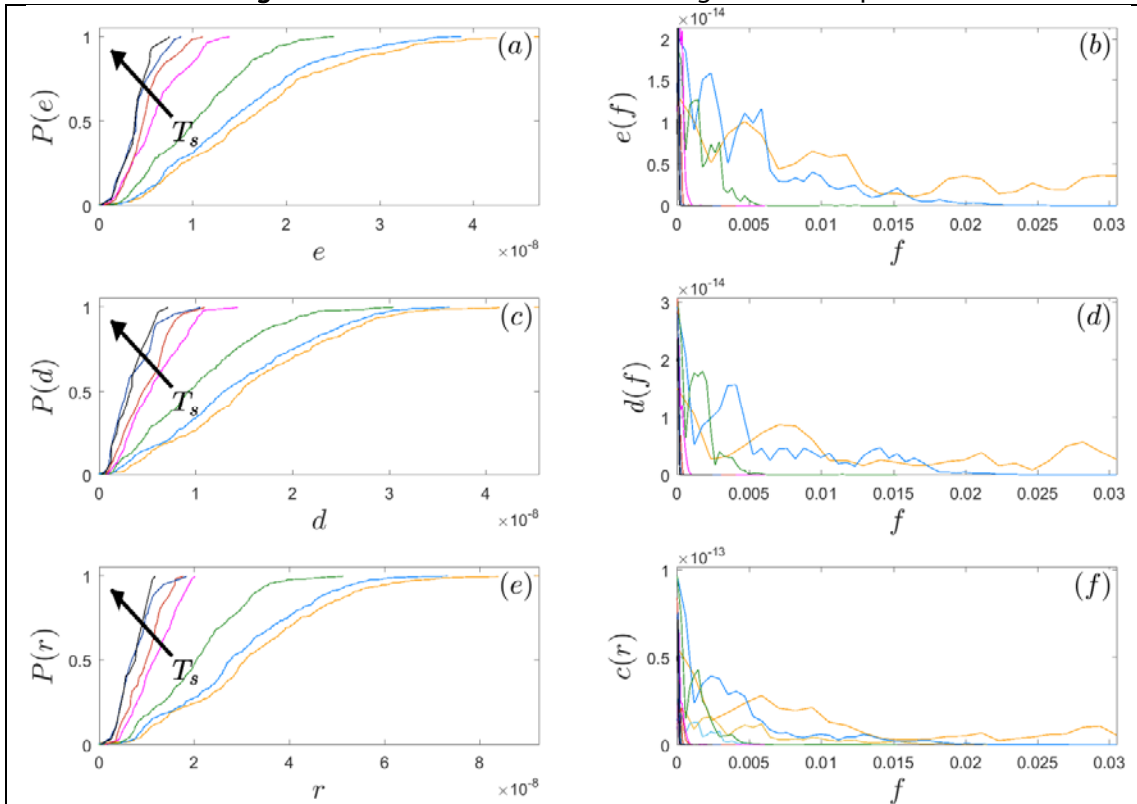


Figure S41 . Data are from run 7. See Figure S3 for explanation.

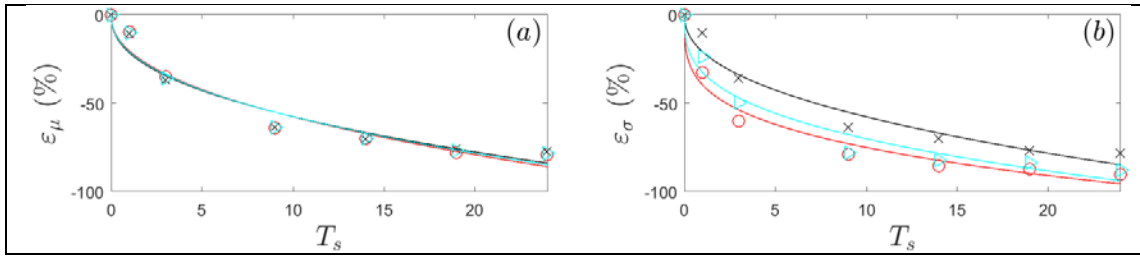


Figure S42 . Data are from run 7. See Figure S4 for explanation.

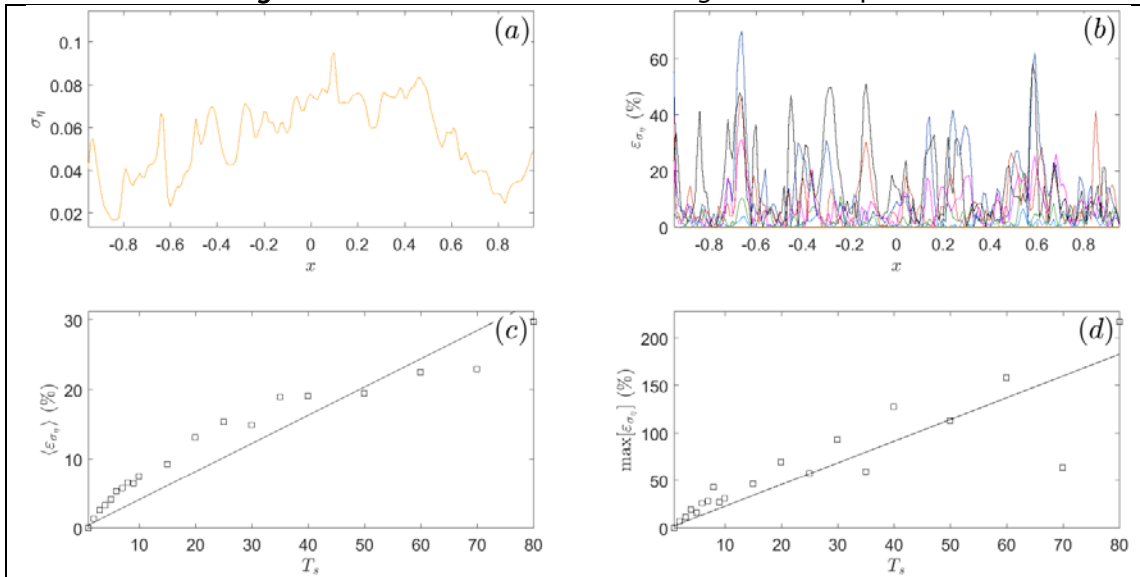


Figure S43 . Data are from run 7. See Figure S5 for explanation.

Run 8

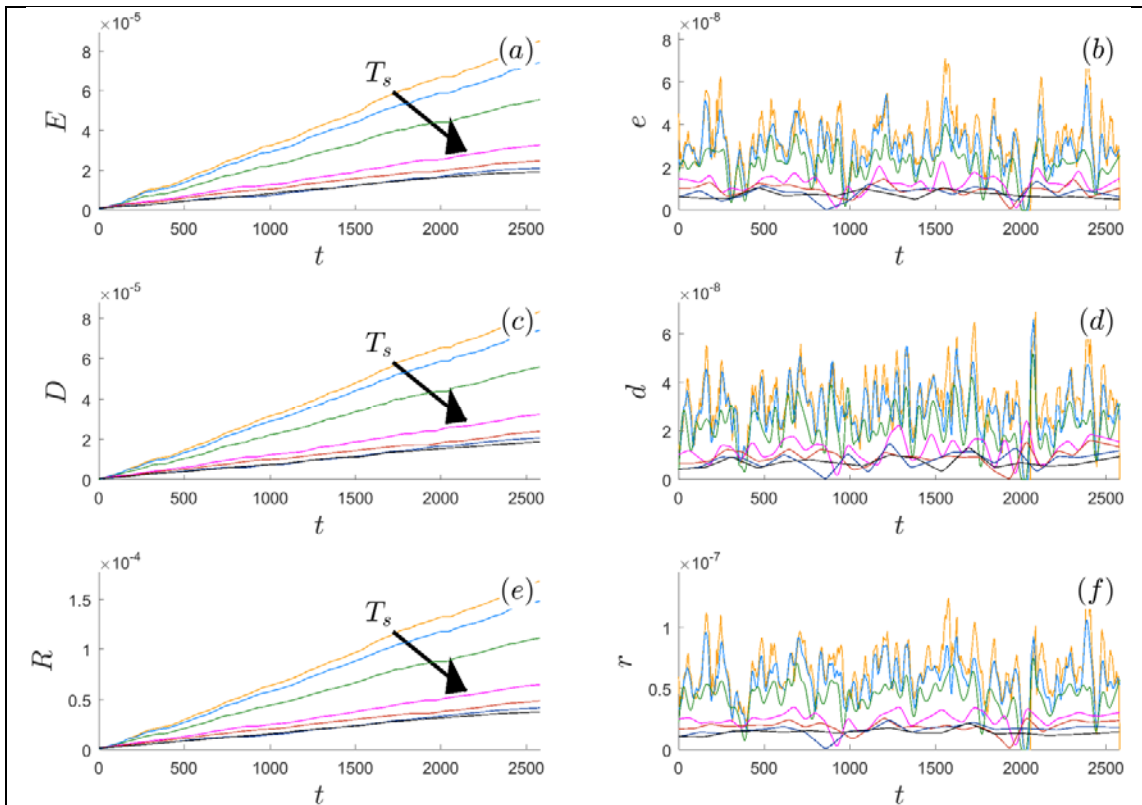


Figure S44 . Data are from run 8. See Figure S2 for explanation.

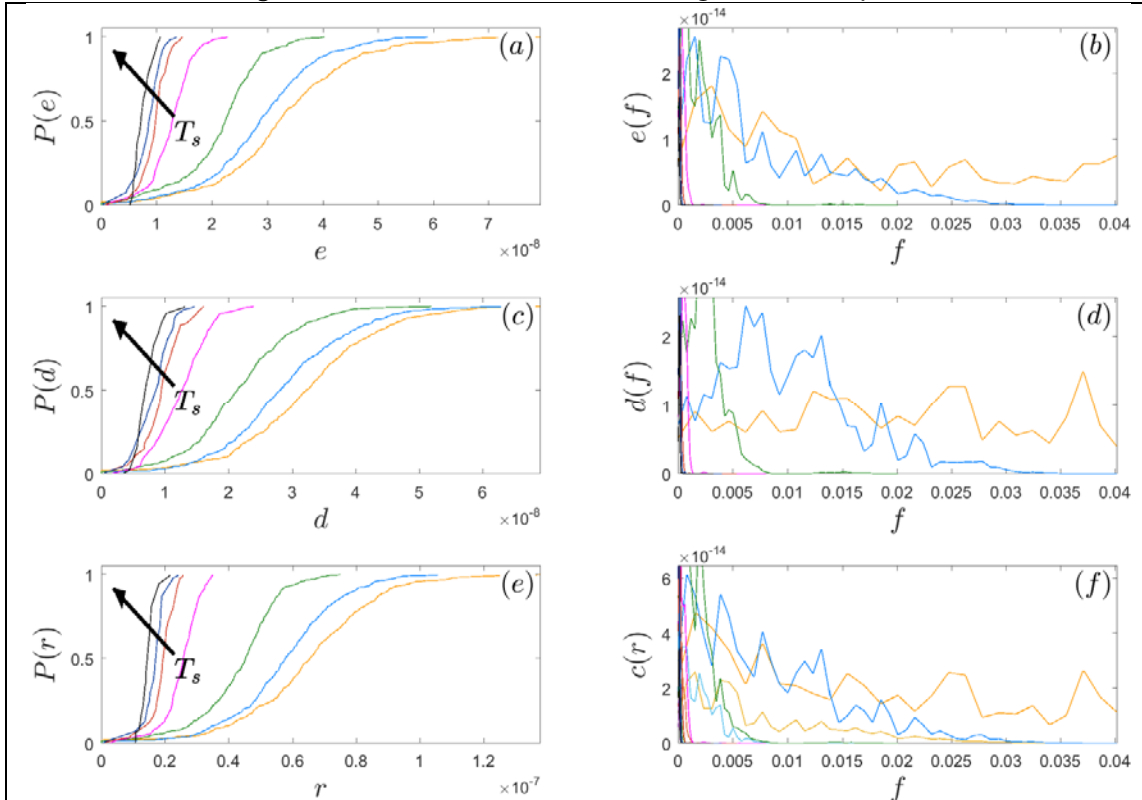


Figure S45 . Data are from run 8. See Figure S3 for explanation.

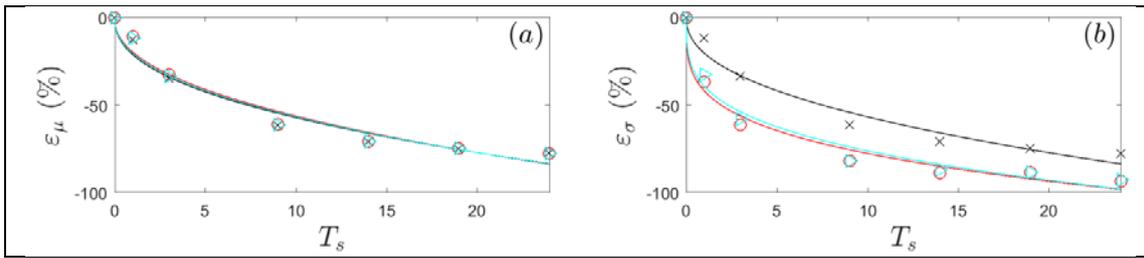


Figure S46 . Data are from run 8. See Figure S4 for explanation.

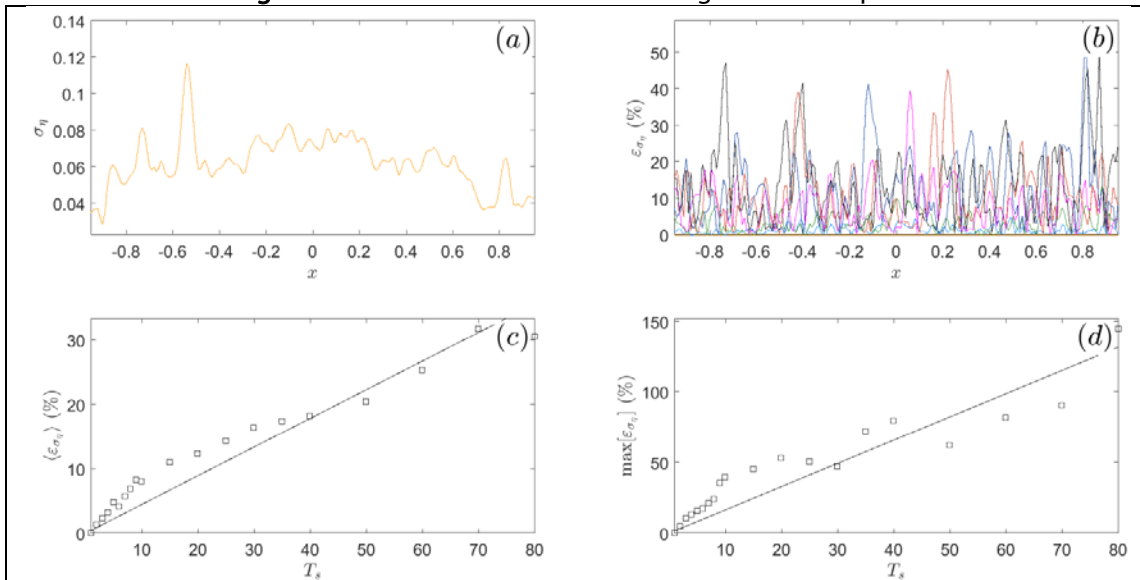


Figure S47 . Data are from run 8. See Figure S5 for explanation.

Run 9

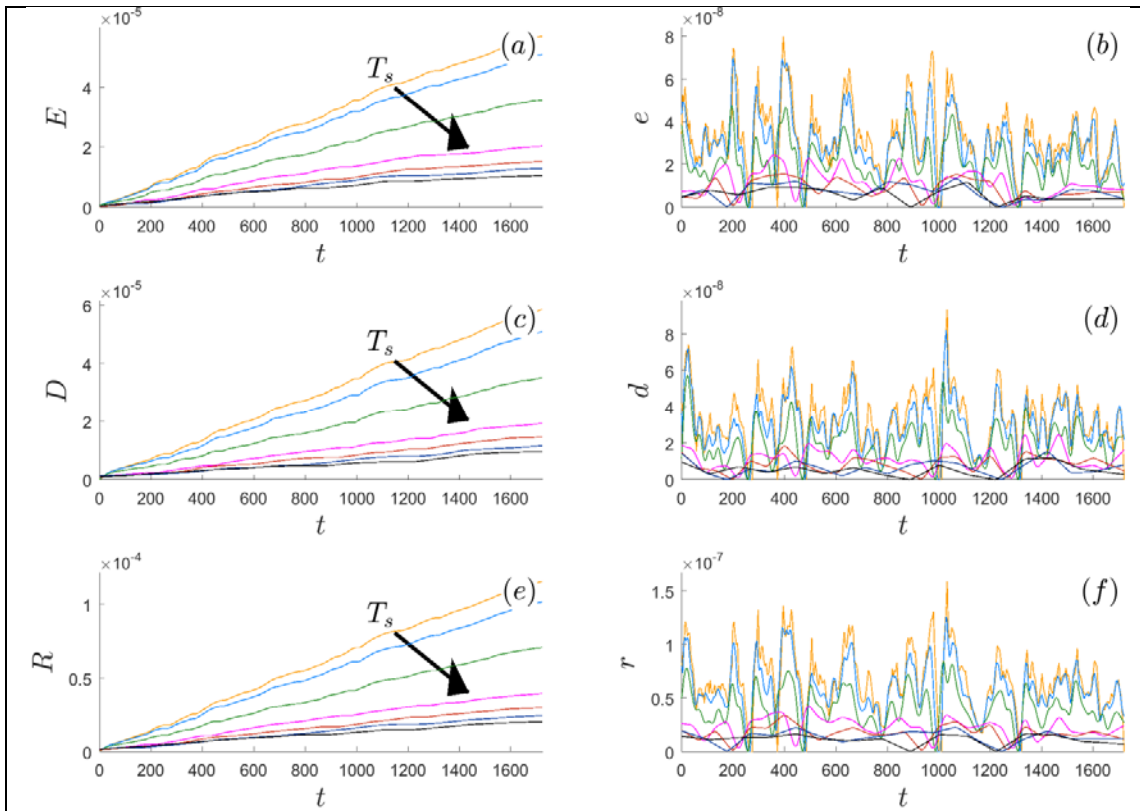


Figure S48 . Data are from run 9. See Figure S2 for explanation.

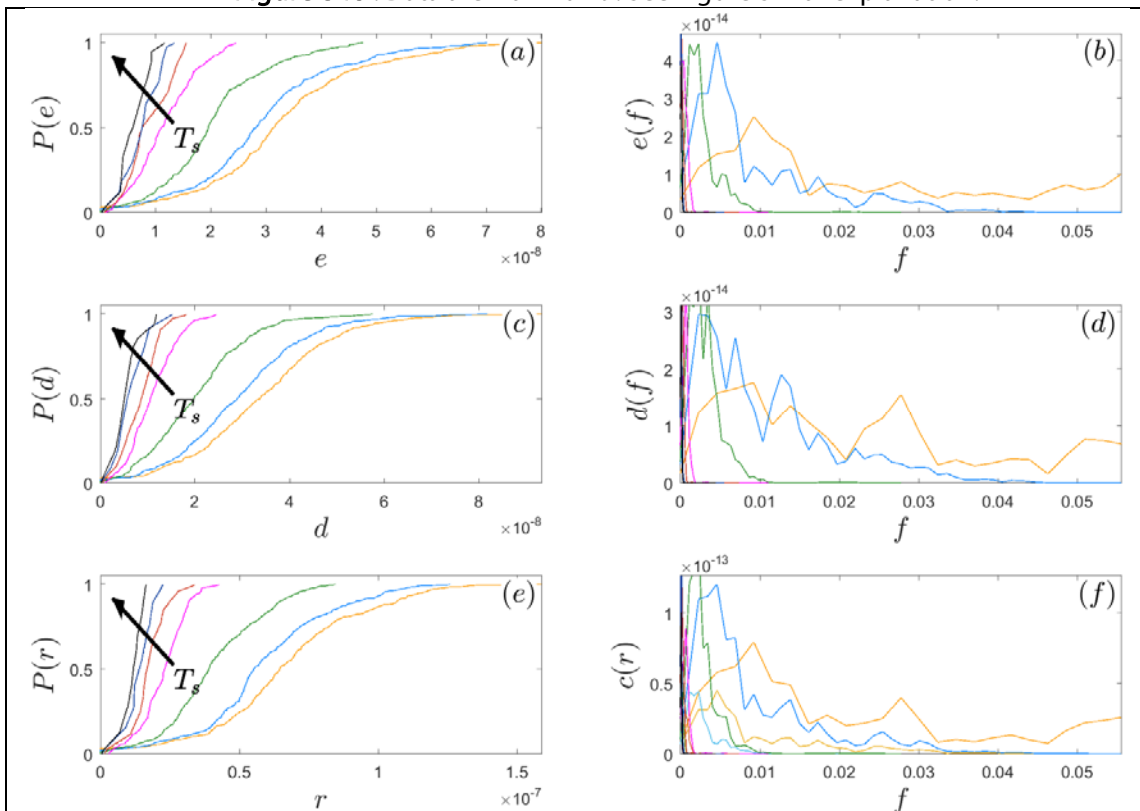


Figure S49 . Data are from run 9. See Figure S3 for explanation.

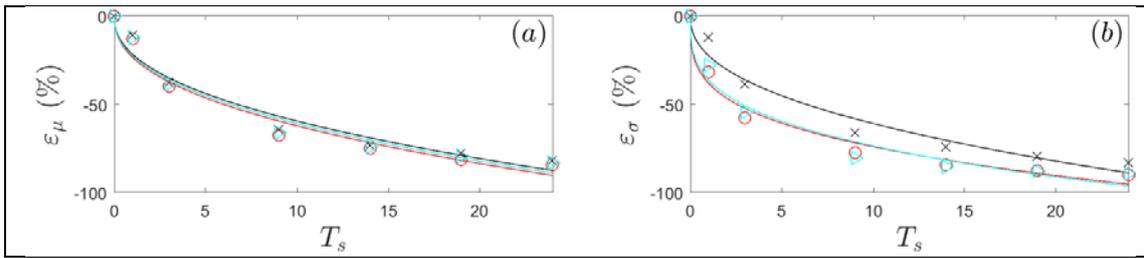


Figure S50 . Data are from run 9. See Figure S4 for explanation.

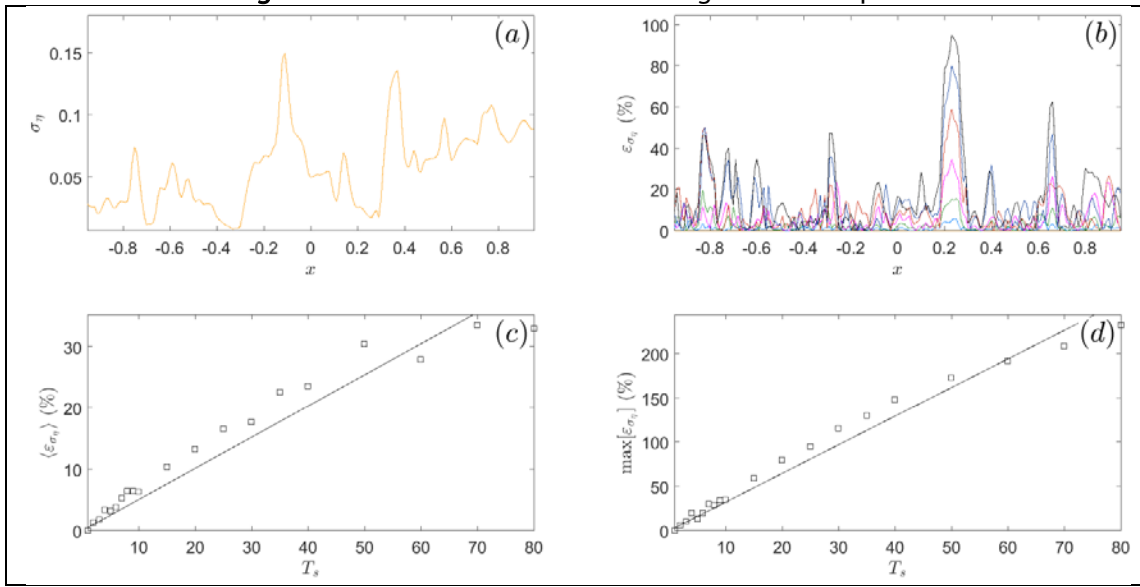
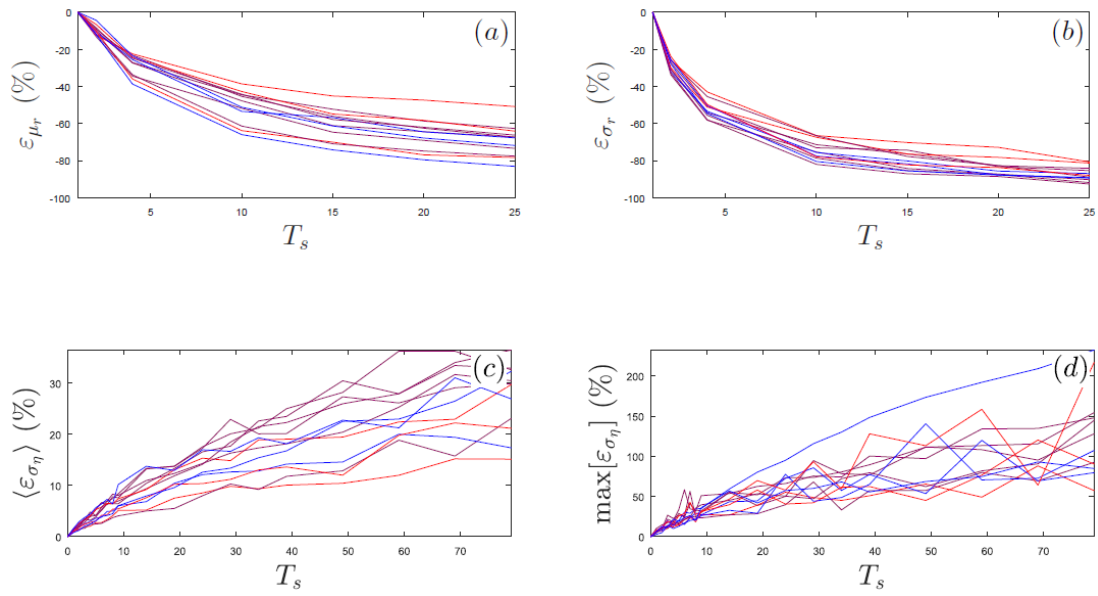


Figure S51 . Data are from run 9. See Figure S5 for explanation.

### Role of the dimensionless flow rate



**Figure S52 .** (a,b) The  $T_s$ -dependent  $\varepsilon_{\mu_r}$  and  $\varepsilon_{\sigma_r}$  for different runs. (c,d)  $\langle \varepsilon_{\sigma_n} \rangle$  and  $\max[\varepsilon_{\sigma_n}(x)]$  as a function of  $T_s$  for different dimensionless flow rate (different colors). The red (blue) curve refers to the  $q=492$  ( $q=778$ ). Intermediate shades are intermediate values of the dimensionless flow rate  $q$ .

### Assessment of the errors in measurements with a sampling time longer than the optimal sampling time

Let us assume that the flume model evolution is  $\lambda_t$  times faster than the real river evolution. At the model-scale, we found that the minimum time interval between two consecutive surveys is  $(\tilde{T}_{s,\min})_M = 4 \text{ min}$  ( $M$  refers to “model”). This sampling frequency guarantees that all the relevant morphological processes of the model are surveyed. This time interval becomes  $(\tilde{T}_{s,\min})_F = \lambda_t \times (\tilde{T}_{s,\min})_M$  at the real-river-scale, where the subscript  $F$  refers to “full scale”. Let us also assume that the real river is characterized by the stream power  $\omega_F$ . For illustrative purposes, we assume that  $\lambda_t = 30$  so that  $(\tilde{T}_{s,\min})_F = \lambda_t \times (\tilde{T}_{s,\min})_M = 30 \times 4 = 120 \text{ min}$ . Moreover, it is assumed that  $\omega_F = 7.2$ .

If a sampling time  $(\tilde{T}_s^*)_F > (\tilde{T}_{s,\min})_F$  is adopted in the field measurements of the real river, the results of this study can help assessing the errors occurred in the measurement process. For instance, we assume that  $(\tilde{T}_s^*)_F = 1440 \text{ min} = 1 \text{ day}$ .

In order to assess the errors occurred in the measurement process, the first step is to evaluate the dimensionless sampling time, namely  $T_s^* = (\tilde{T}_s^*)_F / (\tilde{T}_{s,\min})_F = 1440 / 120 = 12$ .

The second step is to find a run in the present study characterized by a stream power similar to the examined real stream. In this case, Run 7 is characterized by the stream power  $\omega_M = 7.4$ .

The third step is to use the results of our study to obtain the errors of interest. For instance, let us focus on  $\varepsilon_\mu$ , namely the error occurring during the estimation of the mean reworking rate when the sampling time is larger than the minimum sampling time. The relation between  $\varepsilon_\mu$  and  $T_s^*$  is given in Figure S42a (see also Figure S53a for an enlarged view). The curve reported in Figure S53a shows that when

$T_s^* = 12$ , the error  $\varepsilon_\mu$ , is about -60%.

The same procedure can be used to evaluate other errors like  $\varepsilon_\sigma$ ,  $\langle \sigma_\eta \rangle$ , and  $\max[\sigma_\eta]$  from the curves reported in panels b-d of Figure S53.

Summing up, with the adopted  $(\tilde{T}_s^*)_F = 1 \text{ day} > (\tilde{T}_{s,\min})_F = 120 \text{ min}$ , it is found that that:

- 1) the error on the estimation of the mean reworking rate of sediments,  $\varepsilon_\mu$ , is about -60% (see Figure S53a).
- 2) the error on the estimation of the sediment reworking rate variability (through the parameter  $\varepsilon_\sigma$ ) is about -70% (see Figure S53b).

For what concerns the estimation of the bed-elevation variability, it is also found that:

- 3) the spatially averaged error on the estimation of the standard deviation of the bed elevation (the metric  $\langle \sigma_\eta \rangle$ ) is about 5% (see Figure S53c);
- 4) the maximum error along the transect on the estimation of the standard deviation of the bed elevation (the metric  $\max[\sigma_\eta]$ ) can be as high as 30% (see Figure S53d).

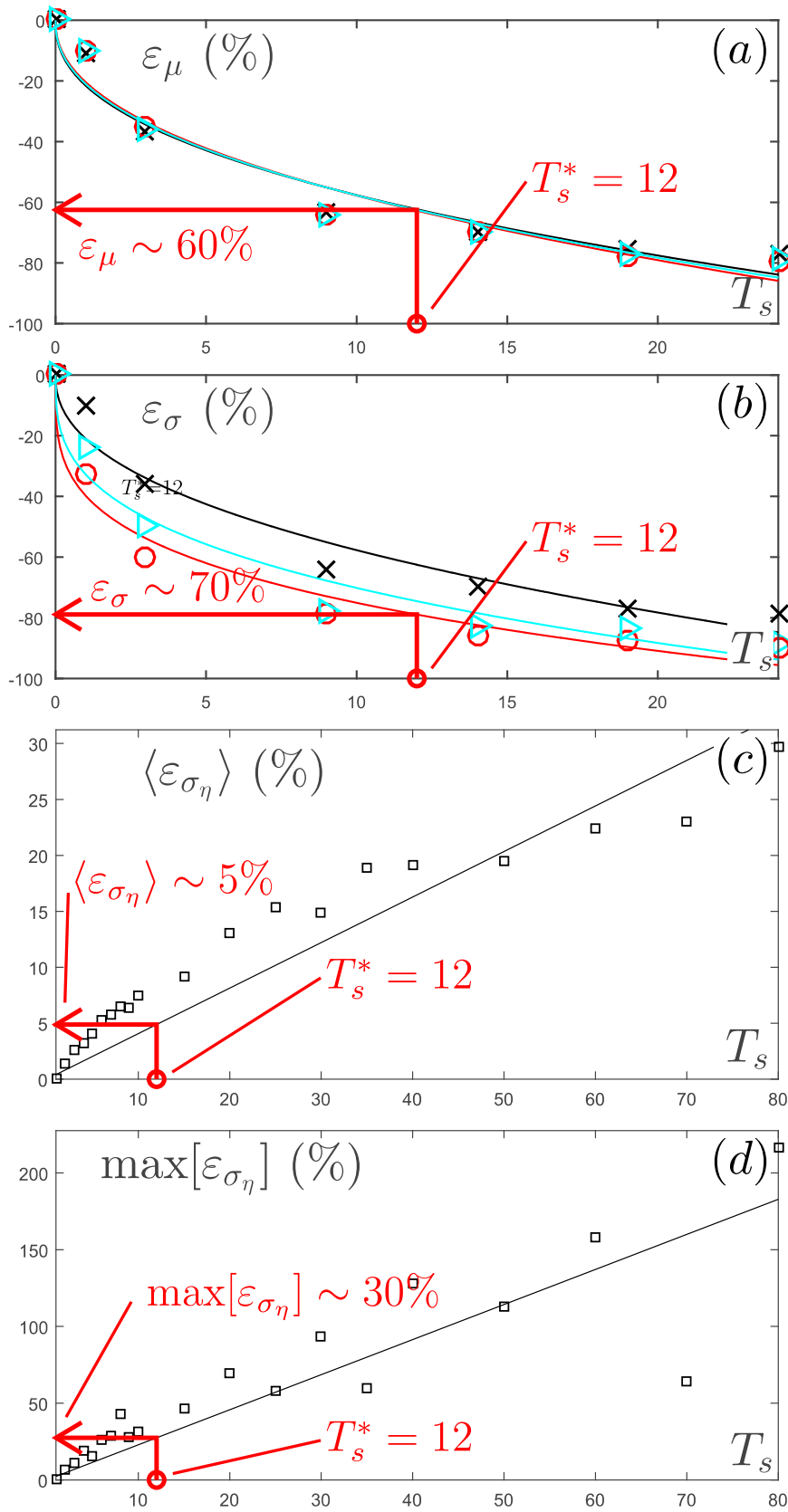


**Figure S53.** Data are from run 7. Panels (a) and (b) are enlarged views of Panels (a-b) of figure S42. Panels (c) and (d) are enlarged views of Panels (c-d) of figure S43.

## References

- Bertoldi, W., L. Zanoni, and M. Tubino (2009a), Planform dynamics of braided streams, *Earth Surf. Processes Landf.*, *34*(4), 547–557.
- Egozi, R., and P. Ashmore (2008), Defining and measuring braiding intensity, *Earth Surf. Processes Landf.*, *33*(14), 2121–2138.